2- P (mix)

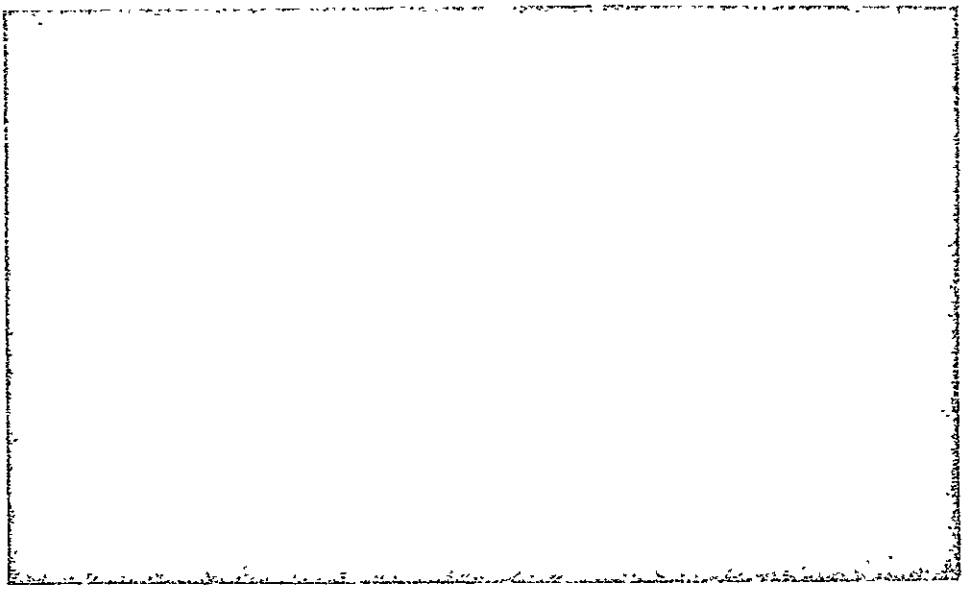

A XEROX COMPANY
PASADENA, CALIFORNIA 91107 • 213/351-2351

CR-114940

Final Report

SOLAR WIND MASS SPECTROGRAPH

Prepared for
National Aeronautics and Space Administration
Manned Spacecraft Center
Space Sciences Procurement Branch
Houston, Texas 77058
Attention: Dr. Don Lind/CB

Contract NAS9-9909

EOS Report 4044-Final 31 December 1970

Prepared by
Lawnie Taylor
SWMS Program Manager

Approved by

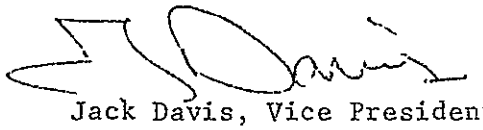

Jack Davis, Vice President and
Manager, Aerospace Systems Division

ELECTRO-OPTICAL SYSTEMS
A XEROX COMPANY

CONTENTS

ILLUSTRATIONS

ILLUSTRATIONS (contd)

ABSTRACT

This final report is submitted in compliance with the requirements of NASA Manned Spacecraft Center Contract NAS9-9909. This report covers the 12-month period of effort from 12 August 1969 to 12 August 1970.

Described in this report are the engineering and performance specifications obtained for a Solar Wind Mass/Charge Spectrograph and a Solar Wind Direction Indicator.

The spectrograph developed in this program is a miniaturized double-focusing instrument designed to demonstrate the feasibility of measuring photographically the mass/charge number composition of the solar wind with a high degree of resolution and sensitivity. The unit is primarily designed to measure mass/charge numbers in the range 1.5 to 4.7; however, it is not limited to this range.

The direction indicator is a self-contained instrument which has been designed to demonstrate the feasibility of determining attitude with respect to the flow direction of an incident ion beam over a range of angles from 15° to 0.25° within an accuracy of 5 percent. The instrument can provide an Apollo astronaut with the capability of adjusting the roll and pitch of the spacecraft within $\pm 0.5^{\circ}$ of the solar wind mean direction.

SECTION 1

SPECTROGRAPH ENGINEERING SPECIFICATIONS

Table 1-1 presents the parameters and aberration coefficients which form the basis for the instrument design. A complete explanation of the symbols and notation used is given in the Appendix.

Figure 1-1 shows a simplified schematic of the spectrograph.

The components of the spectrograph are mounted on an aluminum flat plate with dimensions 10 in. x 18 in. This plate in turn is mounted upon a subplatform structure containing two worm gears, accompanying drive screws, a ball joint, and two flexible cables all of which apparatus provides the means necessary to finely drive the spectrograph platform in either the elevation or azimuth angle directions. The entire assembly mounts inside a 12 in. diameter ante-chamber with the flexible cables connecting to drive shafts which lead to the outside through vacuum mechanical feedthroughs.

Figure 1-2 shows the top view of the spectrograph. Positioned at the forward left corner of the platform can be seen the ion signal monitor sensor which is a grid-grid-plate construction with the center grid at a retarding potential for electrons. The output from this sensor is fed into a Keithley electrometer.

Immediately to the right of the sensor is an ordinary camera shutter with a cable attached for tripping the shutter. This is activated from outside the vacuum system. The shutter mechanism provides the means for controlling the ion beam to the object slit of the spectrograph.

Table 1-1

DOUBLE-FOCUSING MASS/CHARGE SPECTROGRAPH DESIGN PARAMETERS

Dimensionless Physical Parameters			Aberration Coefficients		
c	=	1.00	A_u	=	-1.06
n	=	0.91	A_α	=	0.0011
ϕ_e	=	70.95	A_γ	=	-1.02
ϕ_m	=	102.00	A_δ	=	-0.0039
ϵ'	=	4.92	A_{uu}	=	-1.52
ϵ''	=	-39.00	$A_{u\alpha}$	=	-0.70
I_α'	=	-0.060	$A_{u\gamma}$	=	-0.63
I_α''	=	0.050	$A_{u\delta}$	=	3.59
r_e/r_m	=	0.749	$A_{\alpha\alpha}$	=	-2.19
*D	=	0.311	$A_{\alpha\gamma}$	=	1.39
$\bar{Q}'$	=	0	$A_{\alpha\delta}$	=	0.0075
$\bar{Q}''$	=	0.010	$A_{\gamma\gamma}$	=	0.62
$\bar{R}'$	=	0.286	$A_{\gamma\delta}$	=	2.13
$\bar{R}''$	=	0.010	$A_{\delta\delta}$	=	-0.47
$*L_e$	=	0.294	A_{vv}	=	1.01
$*L_m$	=	1.126	$A_{v\beta}$	=	1.44
Sense	=	Opposit	$A_{\beta\beta}$	=	0.15

*Multiply by 3.937 to obtain linear dimensions in inches.

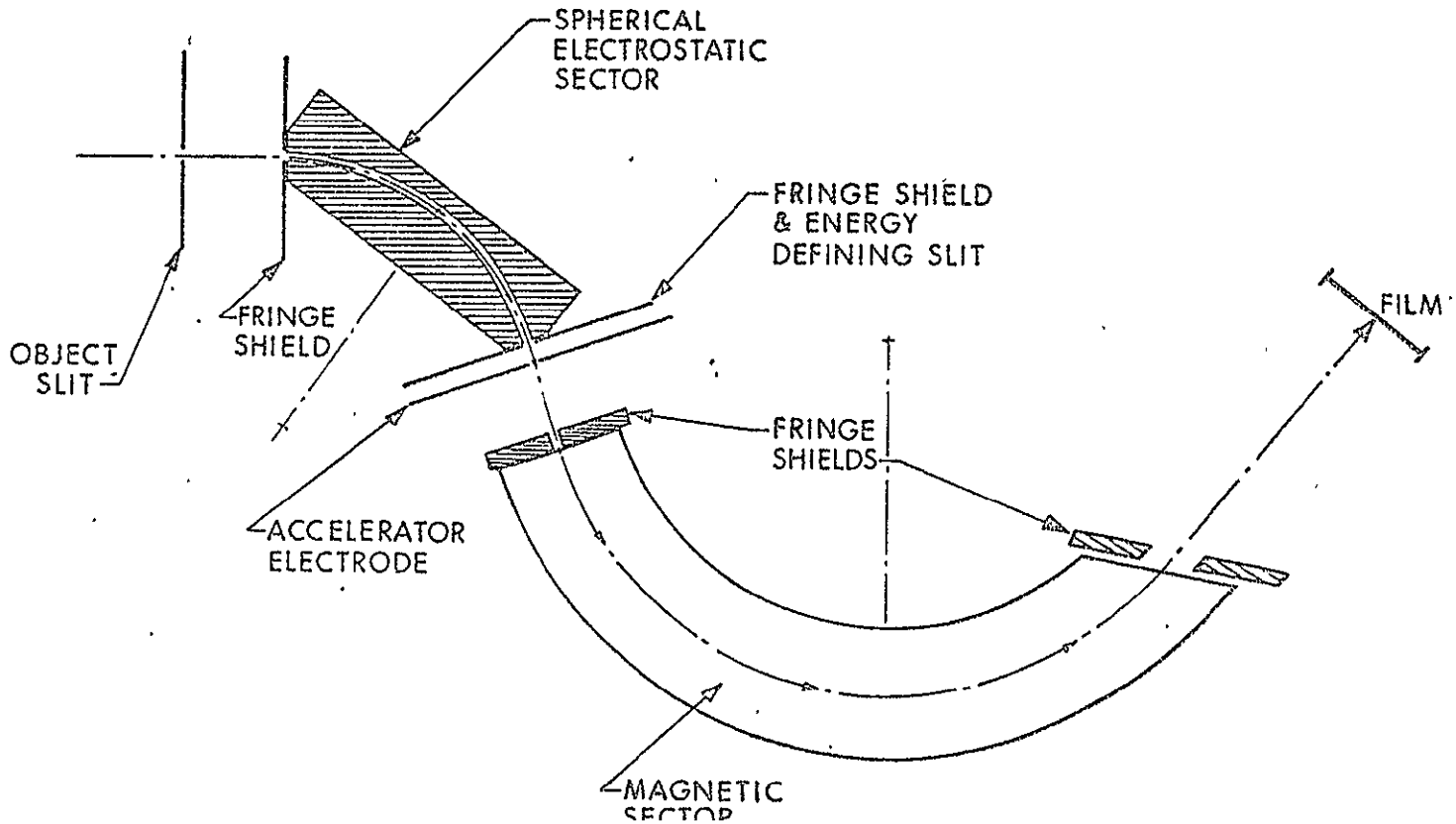

Figure 1-1. Double Focusing Mass/Charge Spectrograph Schematic

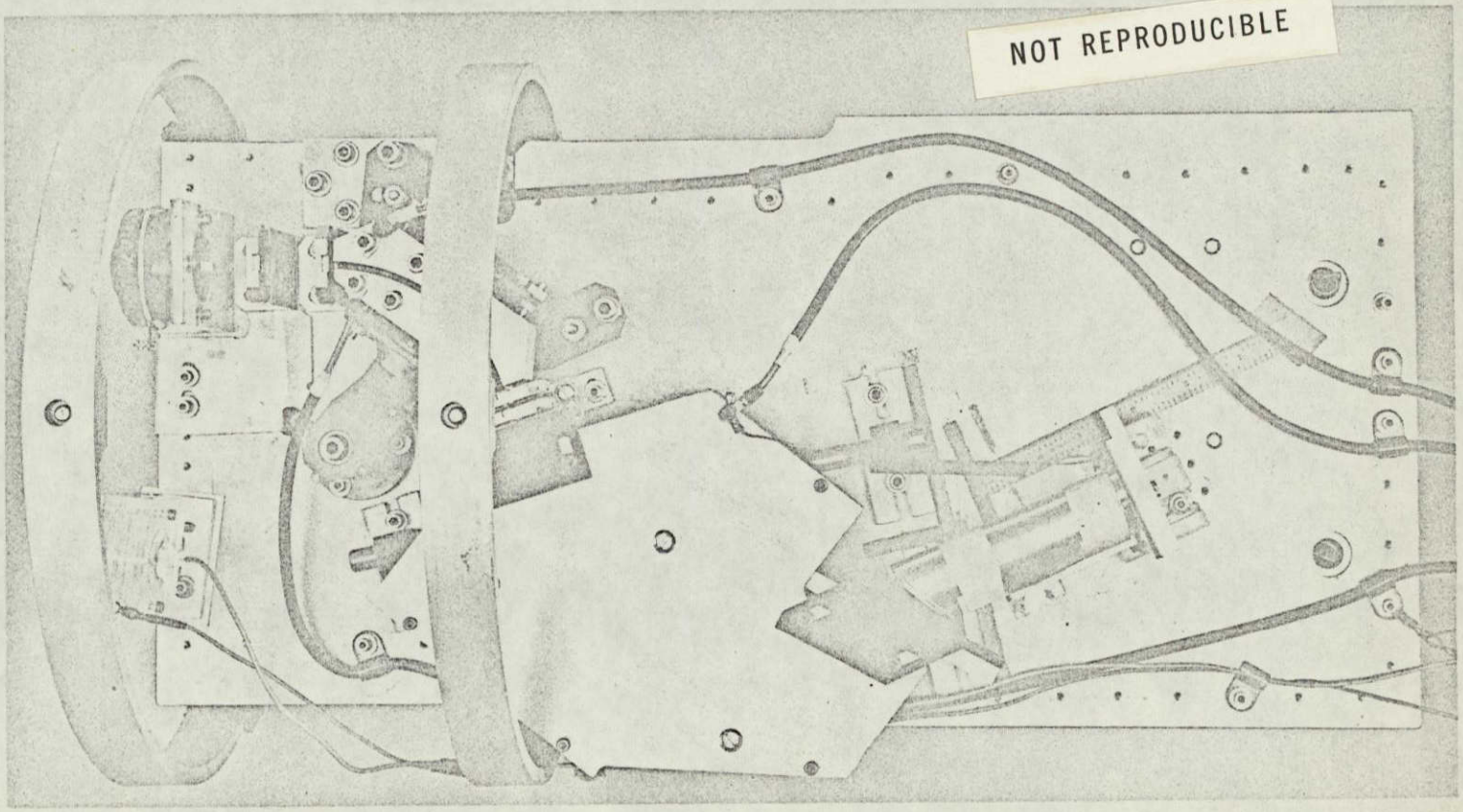

Figure 1-2. Top View of the Spectrograph

The object slit consists of adjustable razor blade edges. The center of the slit is at the height of the center line of the spectrograph which is 1.875 in.

The frings field shield at the entrance face of the electric sector is located 1.100 in. from the object slit, along the line-of-centers. The object slit and fringe field shield mounts can be clearly distinguished in Figs. 1-3 and 1-4. The slit of the fringe shield is constructed identically to that of the object slit, except the width is 0.075 in.

Next, the electric sector with its adjustment mounting can be seen. This gold-plated unit is positioned with its entrance face parallel to the fringe field shield. These two units are separated by 0.075 in. Figure 1-5 describes the dimensional detail of the sector which has a spherical contour on the inner plate surfaces. The mounting mechanism does not appear in Fig. 1-5. This mechanism permits a variety of adjustments, translational, angular, and gap separation, in order to achieve the rather delicate alignment.

Following the sector is another fringe field shield at the output face identical to the one at the input face. Spaced 0.090 in. from this shield is another identical slit except that it is electrically insulated from ground. This comprises the accelerator unit. This unit can be clearly seen in the photograph of Fig. 1-3.

The accelerator looks along the line-of-centers into the magnet entrance face which is spaced 1.120 in. from the fringe field shield. The accelerator plate and the magnet entrance fringe field shunt are located in that spacing. Figure 1-6 describes the inhomogeneous field, low intensity magnet which was used throughout the experiments. All surfaces except those of the magnet material are gold-plated. A high intensity magnet (to extend mass/charge range) of approximately 2860 gauss at the

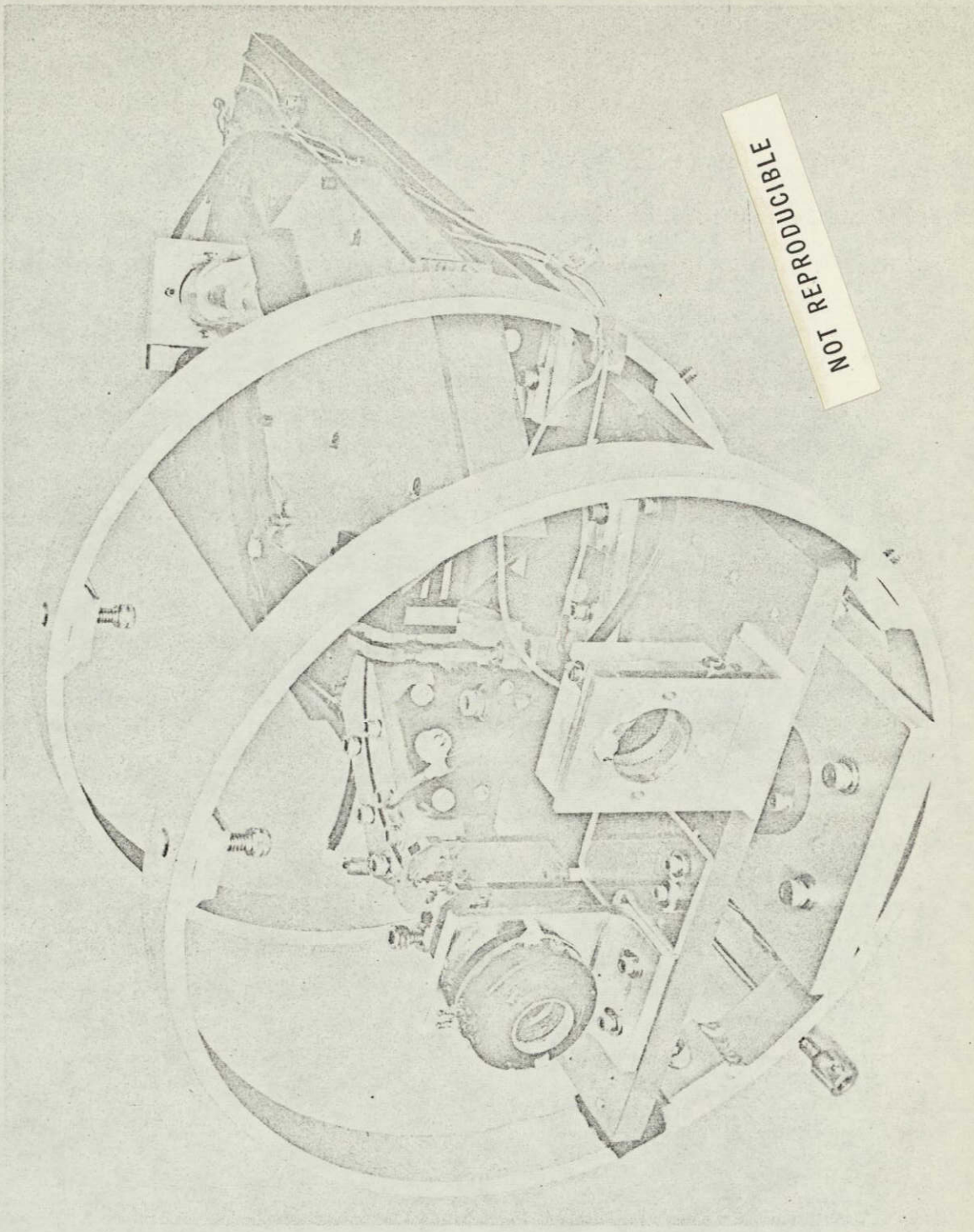

Figure 1-3. Front View of the Spectrograph

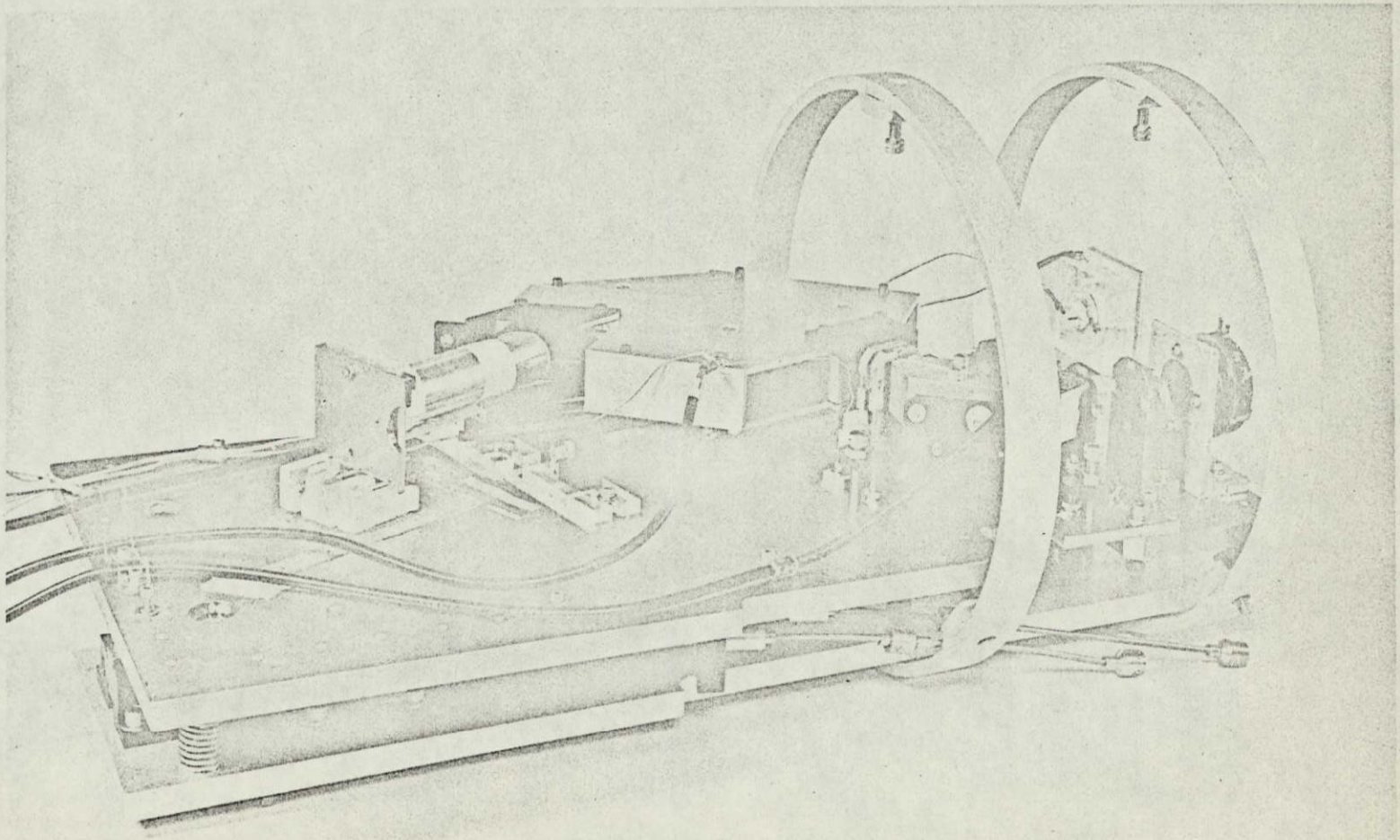

Figure 1-4. Side View of the Spectrograph

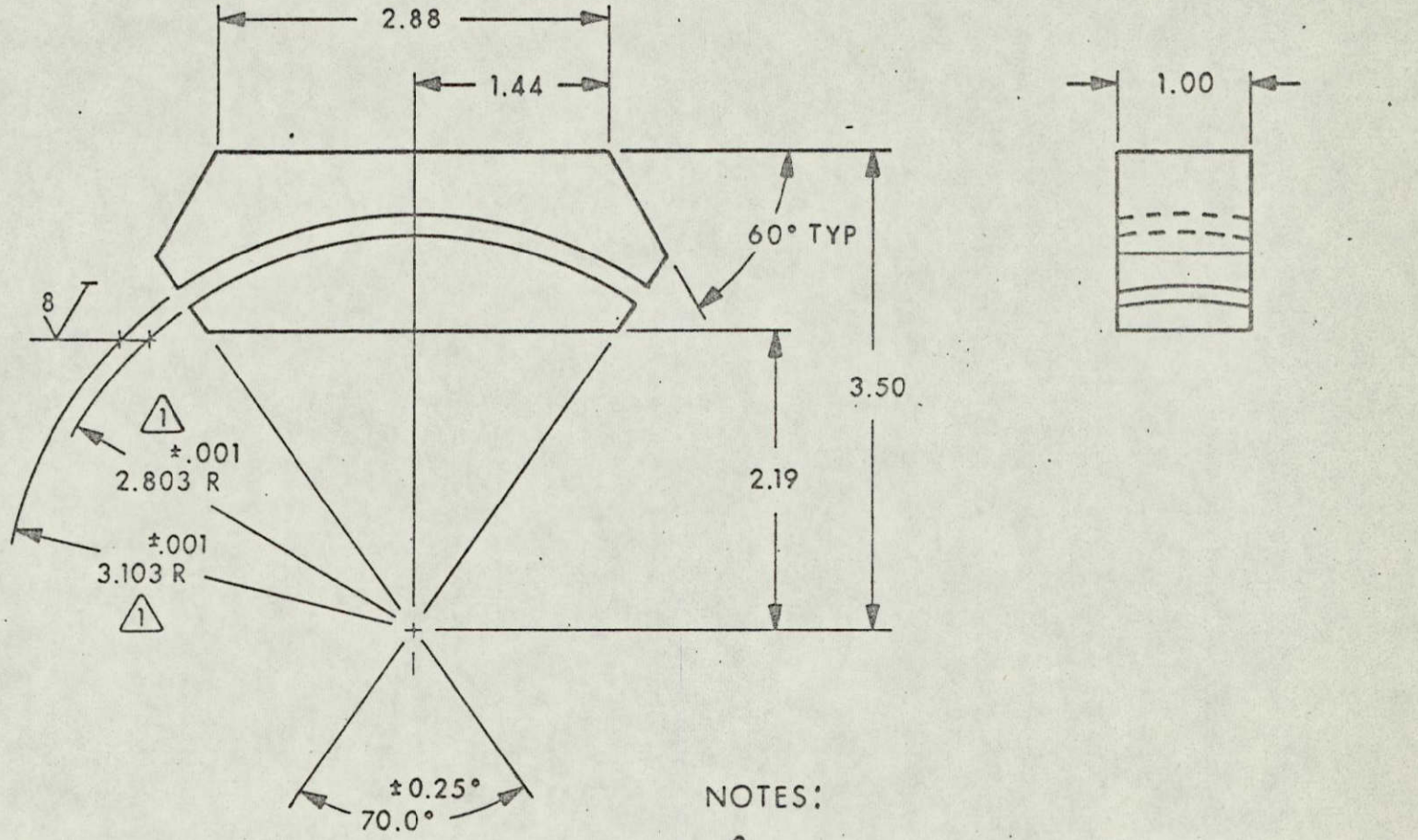

NOTES:

1. SPHERICAL RADII CONSTANT WITHIN 0.0001 OVER 70° ARC SEGMENT
2. MATERIAL: 302-304 CRES - ANNEALED AFTER MACHINING
3. ALL SURFACES GOLD PLATED

Figure 1-5. Spherical Electrostatic Sector

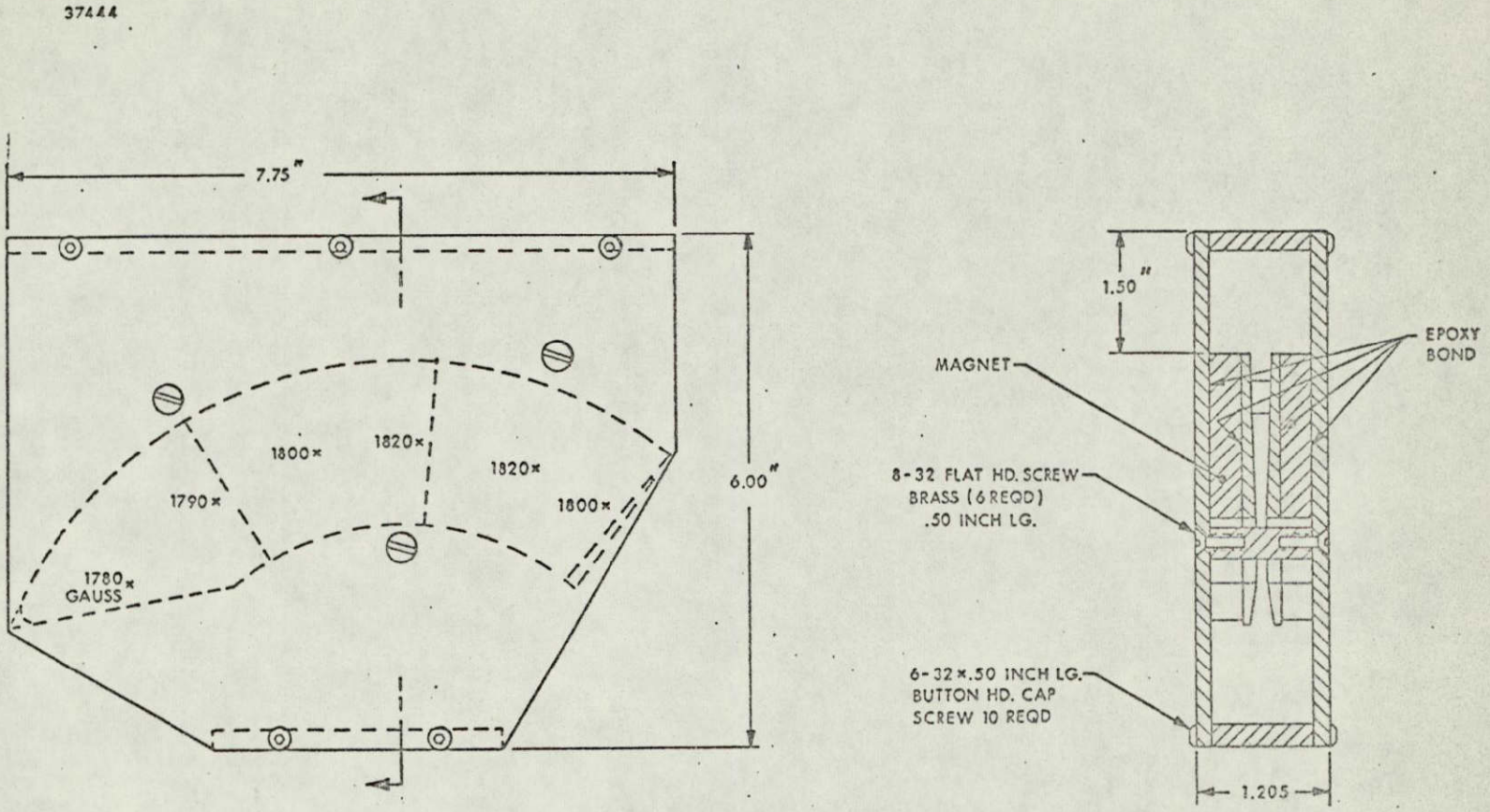

Figure 1-6. Low Intensity Inhomogeneous Field Magnet Mass/Charge

center line with essentially the same structure is shown in Figs. 1-7 and 1-8. The mounting fixture for the magnet (not shown in Fig. 1-6) provides for a fine adjustment parallel to the plane of the accelerator slit in order to align the magnet onto the line-of-centers. Adjacent to the exit face of the magnet is the exit fringe field shunt. The minimum width of the pole faces was determined from computer solutions that provided plots of the trajectories of mass/charge numbers differing from the mean value by ±20 percent but entering the magnet with the same energy. The pole face width can accommodate these extreme trajectories.

The line-of-centers intersects the film at the experimentally determined position of 4.900 in. from the exit face of the magnet. An ion beam is caused to exit the magnet and shunt into a field free tube which extends to the film plane.

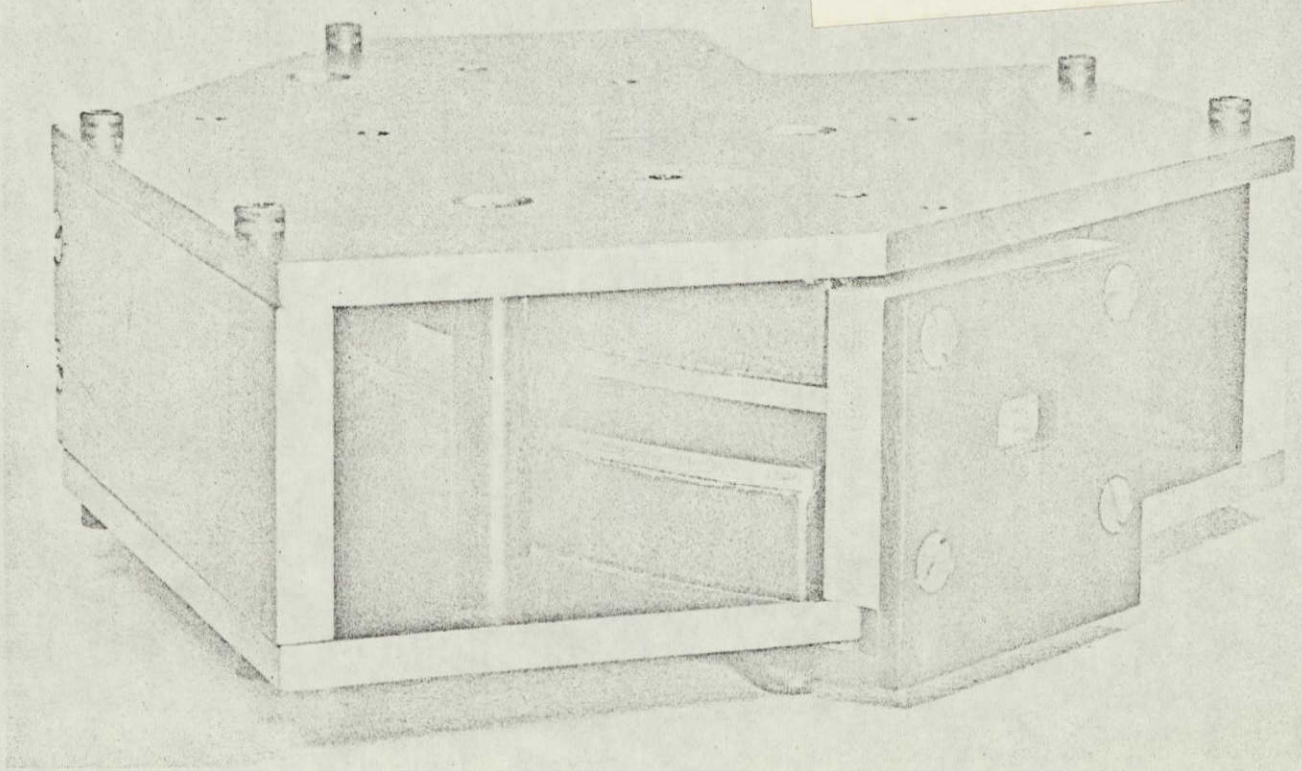

Figure 1-7. View of Inhomogeneous High Intensity Magnet Showing Entrance Shunt (2860 gauss at the centerline)

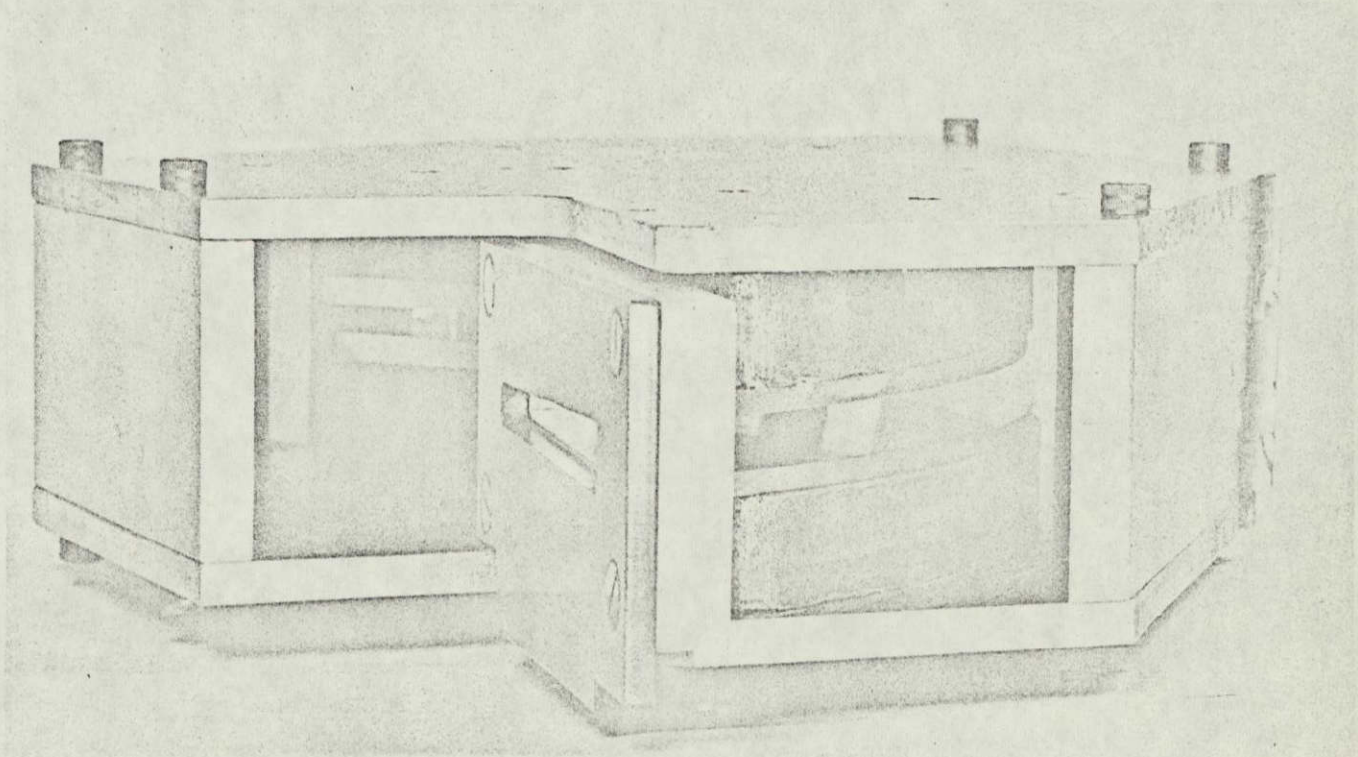

Figure 1-8. View of Inhomogeneous High Intensity Magnet Showing Exit Shunt (2860 gauss at the centerline)

SECTION 2

SPECTROGRAPH PERFORMANCE SPECIFICATIONS

2.1 IMAGING CHARACTERISTICS AND RESOLUTION

Figure 2-1 provides a picture description of the ion beam formed by a 0.004 inch object slit as the beam moves through the spectrograph. The pictures were obtained by positioning strips of film at the specified locations.

The object slit was aligned normal to the incident ion beam; however, it was found that a lower intensity component of the beam was being scattered asymmetrically into the slit at an angle of approximately 0.5^{o}. This might have been caused by the beam collimator located between the source and the spectrograph. The effect can be seen in the beam image as it enters the electric sector wherein a very dark line is accompanied by a lighter line to one side. The beam intensity at the object slit was nominally 2×10^{-13} A/cm^2 and images (1), (2), and (3) in Fig. 2-1 were each exposed for a three-minute period. The images (4) were each exposed for a twenty-second period. The image (2) is widened primarily due to energy dispersion and shortened as the result of axial focusing. The curvature of that image is also due to the spherical field of the electric sector. In (3) the effect of axial focusing is most clearly seen. The three images of He^{+} in (4) were obtained by maintaining the incident beam energy constant (2375 eV) and simply varying the accelerator voltage in the steps 1690, 1700, and 1782 eV. This did not require any change in electric sector potential since the accelerator follows that sector.

The images in (4) of Fig. 2-1 provided the data for determining the mass dispersion of the magnet calculated from a He^{+} mass of 4.003 amu

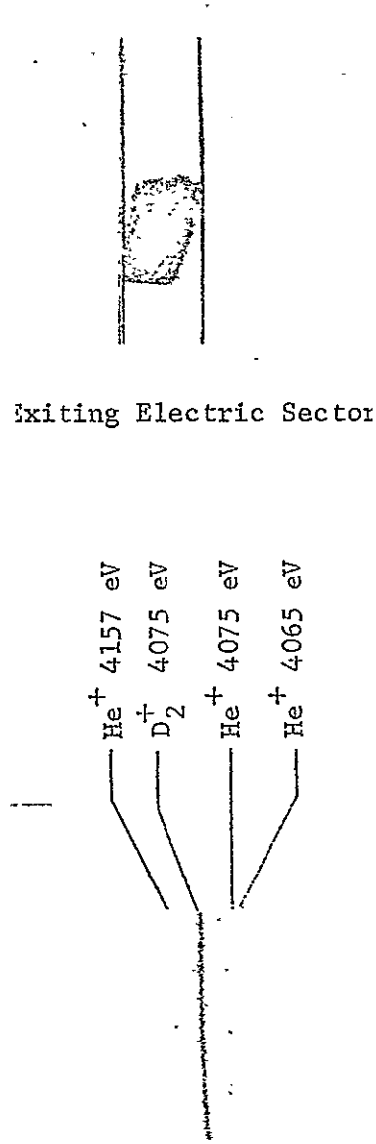

Figure 2-1. Beam Trace Through Spectrograph

and a D_2^+ mass of 4.030 amu. It was found that the separation of two masses differing by 0.01 amu is 1.01 millimeters. Since the magnet radius is 100 millimeters, then the dispersion is precisely A_γ in table 1-1 for which a design value of 1.02 was determined in excellent agreement with that obtained experimentally.

The lines shown in figure 2-2 were obtained by changing the accelerator voltage in increments of 10 eV ranging from 1690 to 1800 eV, inclusive. The exposure time was twenty seconds each line. As in figure 2-1 (4), the incident beam energy was maintained at 2375 eV. The incremental steps in accelerator voltage produced a shift in the position of the He^+ line which would have been observed if the mass had been changed by 1 part in 656. It should be noted that the design resolution curve for a 0.004 inch object slit width given in figure 5 of EOS Proposal 964 predicted a value of 650 for a 1/4 degree acceptance half-angle.

Figure 2-3 shows lines of H_2^+ which has a mass/charge number of 2. The reason for the appearance of a double line is not understood. Figure 2-4 was obtained with a beam intensity of 2×10^{-13} A/cm^2 for 20 seconds.

Figure 2-2. 12 lines of He^+ in 10 eV increments - range 4065 to 4175 eV, demonstrates resolution of 656 with 0.004 inch object slit

Figure 2-3. H_2^+ lines with energies (left to right) 8317, 8237, 8157 eV

Figure 2-4. Demonstrates effectiveness of image intensification in mass spectrography (using channel multiplier device)

2.2 SC.7 PHOTOGRAPHIC FILM

The Kodak-Pathe' SC.7 film which is being used is manufactured in France. This film is the most ion-sensitive emulsion available. Its superior sensitivity results from the centrifuge method by means of which the emulsion is deposited thereby allowing a minimum use of gelatin.

2.2.1 HANDLING CHARACTERISTICS

The film is produced in strips of 35 mm by 180 mm. The emulsion has not been observed to peel or flake either before or after its use. The film strip does buckle significantly when placed in vacuum; however, this is completely prevented by holders which lock the strip along the long edges. Further, the buckling can be removed by simply soaking the film in water for a minute or so after which it becomes very pliable.

SC.7 film is extremely pressure sensitive which requires that it be handled carefully so as to avoid touching the emulsion surface. Many attempts to process the film have resulted in a procedure which has proven to be adequate. Processing is carried out in a closed plastic box which is constantly flushed with dry nitrogen in order to eliminate any significant oxygen atmosphere. The absence of oxygen appears to result in a higher transmission background. A 15-watt lamp with a Kodak B-9 filter is located four feet from the working platform. Temperatures ranging from 20° to 25°C have been satisfactory. The processing steps that have been found to be most consistent in results and yet simple are as follows:

a. Soak in distilled water to render film specimen pliable (2 minutes).

b. Develop in Ilford D-19 for 1 minute 54 seconds, translating the film (or rotating a beaker) slowly during this period.

c. Immerse in distilled water stop (no specific) for 15 seconds.

c. Fix in Kodak rapid fixer for 1.5 minutes, translating the specimen (or rotating a beaker) slowly during the period.

e. Rinse in stagnant distilled water, three separate washes.

It should be noted that the SC.7 film must be handled in either safe light or no light conditions at all times prior to completion of fixing step. Also, the developed portions of the film consist of a powdery layer, a portion of which can be rubbed off. To prevent this, Kodak recommends a lacquer application which will essentially seal the surface.

2.2.2 SENSITIVITY

In the EOS Technical Proposal 964 a derivation was presented in order to predict the detectable levels of ion flux for the SC-7 film. In Fig. 9 of that proposal calculations were made to determine the flux required to produce a clearly visible image.

Experiments have been performed to measure the minimum detectable integrated flux of 5 kilovolt helium ions. A barely detectable image was obtained at an integrated flux value of 3.2 by 10^5 ions/cm^2. This is to be compared with the predicted value from the curves of Fig. 9 (EOS Proposal 964) of 4.8 by 10^5 ions/cm^2 for singly ionized helium.

The development of an image intensification technique deferred any further investigation of minimum detectable levels.

2.3 IMAGE INTENSIFICATION

An attempt to detect integrated flux levels of magnitudes below the capability of SC.7 film alone has resulted in the development of an image intensifier-film technique, the effectiveness of which has been demonstrated with success as evidenced by an ability to detect any ion mass at integrated flux levels extending to below 500 ions/cm^2.

A schematic of the concept is shown in Fig. 2-5. It consists of a channel plate electron multiplier interposed between the incident ion beam and the film. Figure 2-6 is a photograph of a demonstration unit. The channel plate is a Bendix Spiraltron Bundle Model 5205X.

Ions incident upon the channel plate produce secondary electrons in the unit channels of which there are 1530 distributed over an area of 0.2 cm^2 in the Bendix device. The secondary electrons are accelerated towards the opposite terminus of the channel producing more secondaries to the extent that electron gains in excess of 10^6 can easily be achieved, depending upon the voltage (nominally 2500 volt) across the device. Therefore, an incident ion will produce a spot on the film which is the shape and size of the unit channel. In the present instance, the unit channels are 0.003 in. in diameter. Figure 2-4 was obtained with a beam intensity of 2×10^{-13} A/cm^2 for 20 seconds through a 0.004 slit placed in front of the unit of figure 2-6. The background counts correspond to the rate of 10 per second.

The most obvious advantage of this technique is that it can detect on film flux intensities in the particle counting range. For example, a channel plate - film detector was exposed for 10 milliseconds to a 5 kilovolt helium ion flux of 3.6 by 10^4 ions/cm^2-sec. The area of film exposed was 0.025 cm^2. The result was the formation of nine spots distributed over the exposed area of the film, each spot having the contour of the unit channel. One spot, located outside the exposed area, was

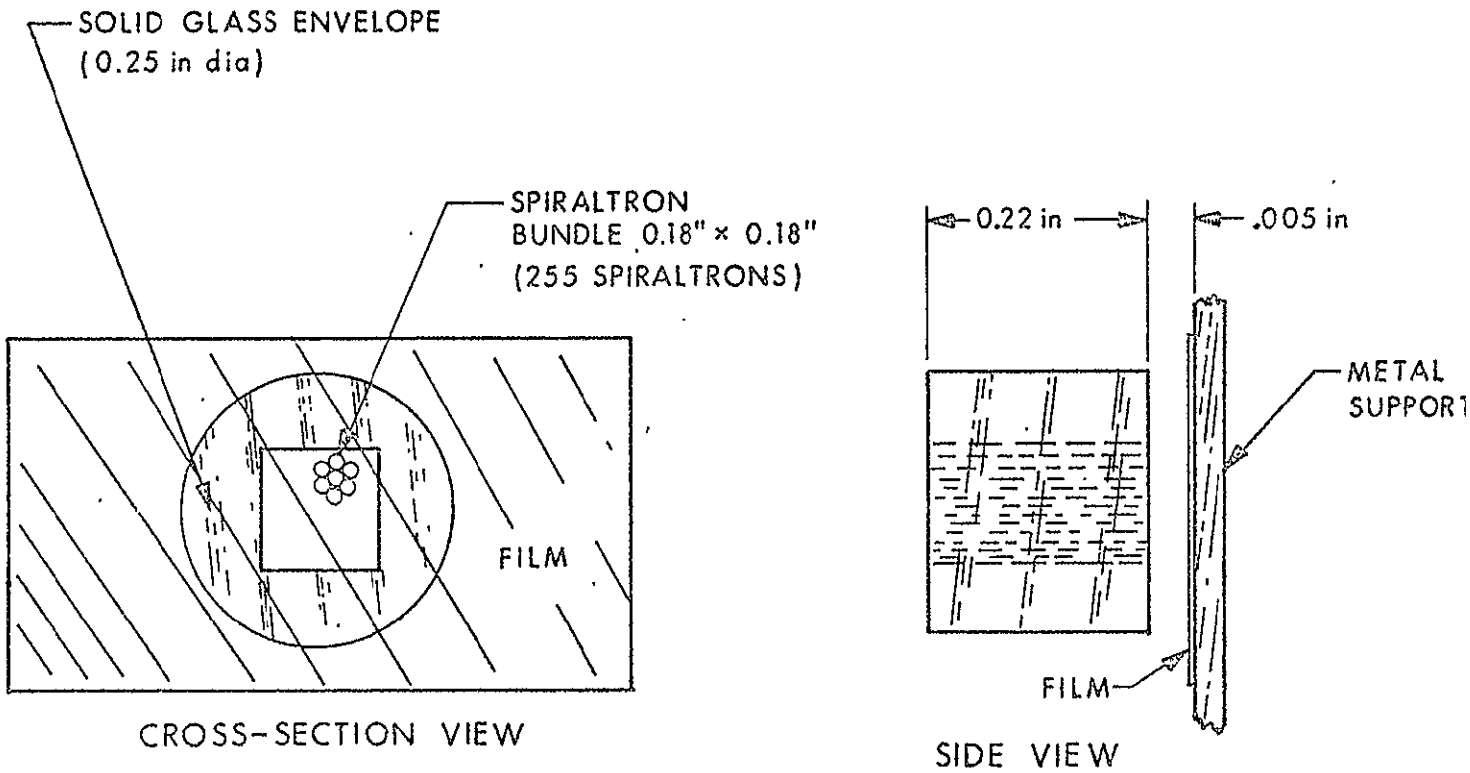

Figure 2-5. Schematic of a Bendix Spiraltron Bundle Model 5205X Containing 255 Spiraltrons (1530 Channel Multipliers) Used as a Channel Plate-Film Ion Detector

57091

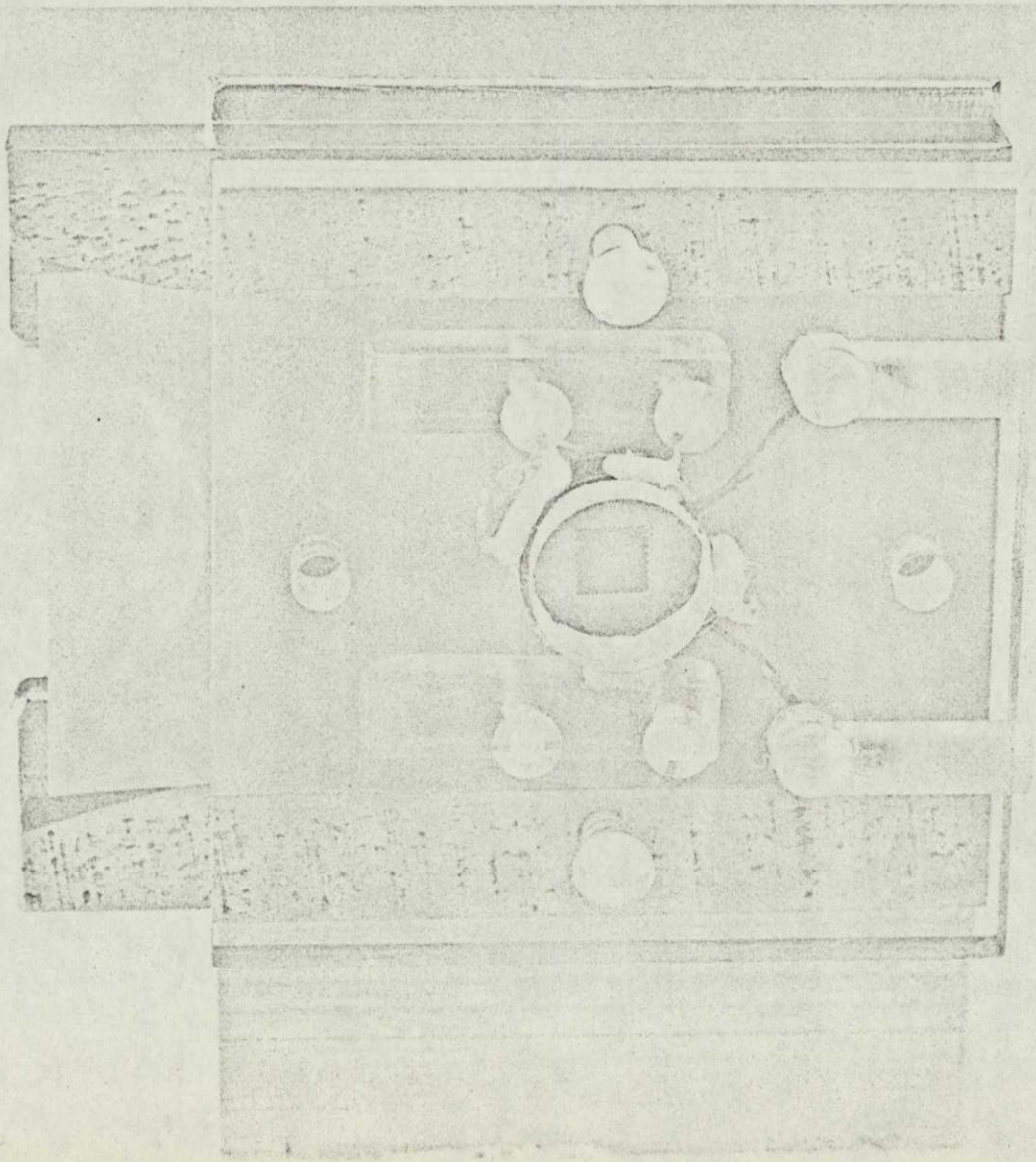

Figure 2-6. Demonstration Channel Plate-Film Detector Unit

identified as a noise count. The nine counts obtained in 10 milliseconds over 0.025 cm^2 amounted to an instantaneous current density of 5.8 by 10^{-15} amp/cm^2 which correlated well with the average current density of 6.8 by 10^{-15} amp/cm^2 as measured by a grid-collector sensor input to a Keithley electrometer.

A second very important advantage of the channel plate - film detector is that the film only sees electrons of fixed energy. Therefore, the detector is rendered insensitive to the mass, charge, and energy of the incident ion provided the ion is sufficiently energetic to produce a secondary electron in a unit channel. Particle energies in the solar wind are adequate for this purpose. Thus the necessity for calibrating the film is eliminated.

A third feature takes advantage of the fact that the image has the shape and size of the unit channel. This can be a very important method for discriminating between an image resulting from only a few counts and other background that might be on the film.

In order for this image intensification technique to be useful in high resolution mass/charge spectrography it will be necessary to obtain channel plates of much greater density, or, specifically, a channel center-to-center spacing of 0.0005 in. which would allow a spatial resolution close to 0.001 in. The plate dimensions should be approximately 4 in. by 0.36 in. by 0.050 in.

2.4 THE ELECTRIC SECTOR

The energy dispersion (D) of a spherical electrostatic analyzer is given by the equation:

$$D = (1 - \cos \varphi_e) + \frac{d \sin \varphi_e}{r_e}$$

where

φ_e is the sector angle

d is the distance from the sector output

r_e is the sector mean radius of curvature

Therefore the trajectories of two particles having energies that differ by the energy deviation (or fractional energy change) δ are separated by a distance $\delta r_e D$ at the position d.

Measurements of current transmission at the exit fringe field shield slit as a function of helium ion energy were made as shown in Fig. 2-7. The potential across the sector plates which were separated by 0.110 in. was 199.7 volts applied as a positive and a negative potential such that the center of the sector gap was at ground. The position of the exit fringe field shield slit was 0.075 in. from the sector boundary. The slit width was 0.075 in. Therefore, d = 0.075 in., and $\delta r_e D$ = 0.0375 in. Since r_e = 2.949 in. and φ_e = 71°, the equation above gives D = 0.698. It follows then that δ = 0.018 which is in excellent agreement with the measured value at half maximum in the curve of Fig. 2-7. The analyzer constant, i.e., the ratio of incident energy to sector potential, is 11.9.

The current detector was then replaced by film strip to determine the pattern at the exit slit for the beam with energy deviation ±0.018. The radial spread was measured to be 0.055 in. That is, the beam originating at a 0.004 in. object slit was moved from center by this amount at the sector exit due to the 1.8 percent change in energy. The helium ion flux intensity used in these experiments was approximately 10^6 ions/cm^2-sec.

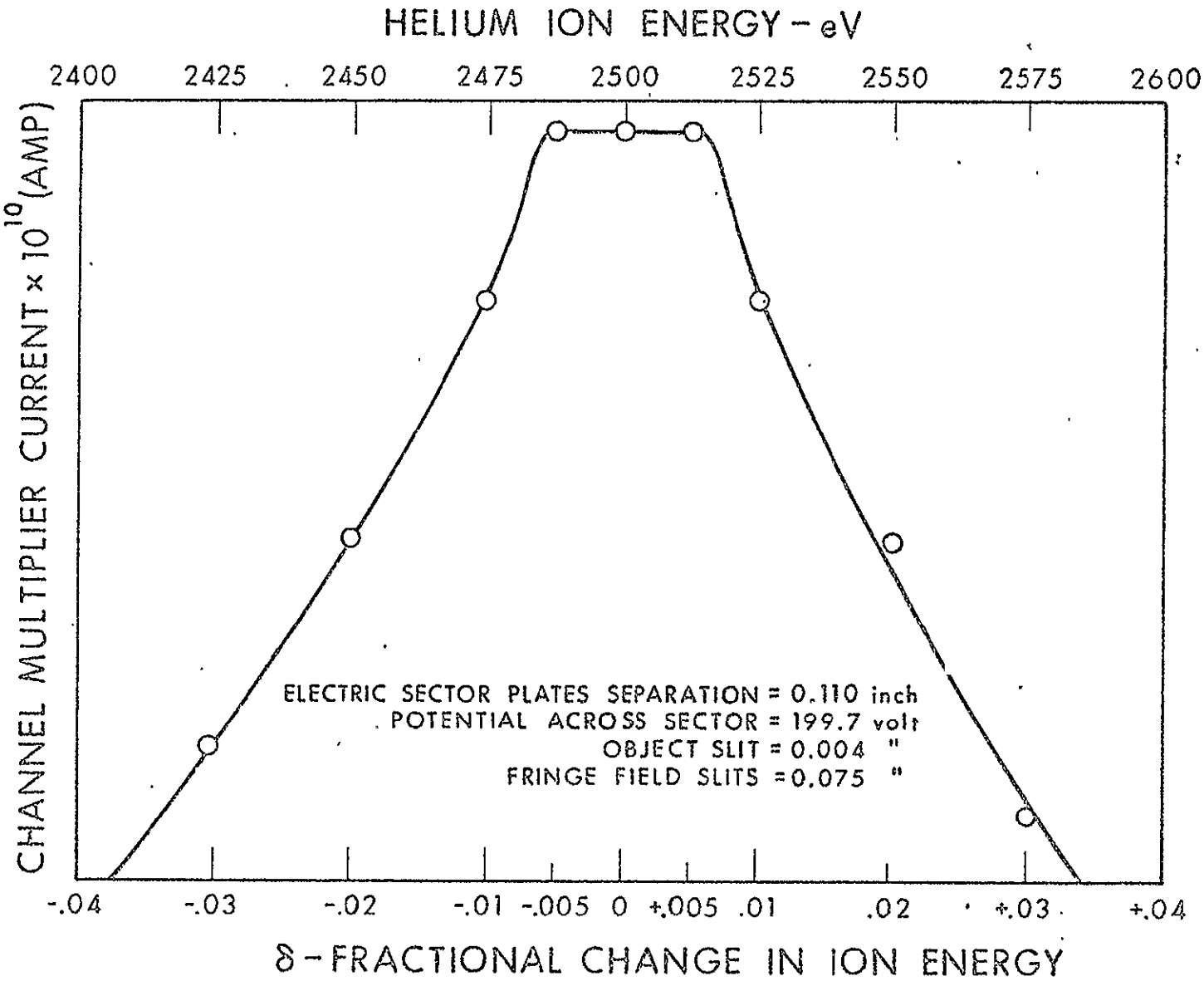

Figure 2-7. Transmission versus Energy Deviation Through the Electric Sector

2.5 THE ACCELERATOR

This unit is an innovation in spectrograph design. The accelerator has two functions. The first is to provide a means of 'tuning' the particle energy such that the trajectory will coincide with the central orbital path in the fixed magnetic field. The second is to more or less collimate the beam since it would be ideal to have a perfectly parallel beam entering the magnetic sector.

With a negative potential of 5000 volts applied to the accelerator electrode, the effects of collimation were clearly evident when the image radial spread of 0.030 in. at 1.150 in. from the exit slit was compared with that of 0.055 in. at the exit slit position without an accelerating field.

For optimum image focusing, it was found that a ratio of accelerator-voltage/incident energy equal to 0.72 was desirable.

2.6 THE MAGNETIC SECTOR

It is necessary to maintain the magnet at the same potential as the accelerator plate in order to preserve focusing conditions. The insulation used to float the magnet must be capable of withstanding 10 keV in vacuum because the slightest breakdown can produce light flashes in the insulation which in turn can result in exposure of the film. The Delrin bushings that support the magnet structure on the mounting fixture were found to be inadequate in preventing high voltage arcing so the mounting fixture feet were changed to plexiglass. Even with the plexiglass considerable care had to be exercised in removing any traces of oil or grease (e.g. resulting from the hands) from the insulation.

After prolonged periods of testing the spectrograph in the vacuum antechamber, the performance of the instrument with respect to image quality

would deteriorate. It was found that oil vapor from the diffusion pump was depositing upon the pole faces of the magnet and evidently causing a build-up of surface charge. Flushing alcohol over the pole faces was sufficient to restore the original image quality.

2.7 THE VELOCITY TUNER

The design of the velocity tuner consists of a parallel-plate energy-per-unit-charge analyzer with dimensions 6 in. long, 2 in. wide, and 1 in. plate separation (H). The input and output slits are located in the same plate and are spaced L = 4 inches apart. The analyzer constant is given by the simple expression L/2H = 2. Therefore the incident-energy-per-unit-charge, U_o/Ze of an ion flux can be determined by:

$$U_o/Ze = 2V_{tuner}$$

where V_{tuner} is the voltage across the analyzer plates.

A test model was fabricated with gold-plated mirror finishes for the electric field bearing surfaces. A phosphor-coated glass slide was placed over the output slit as a beam sensor. The tuner model was mounted in a glass vacuum system in such a manner that the orientation of the input slit with respect to a collimated electron beam could be adjusted externally. By controlling the energy of the electron beam and the voltage across the analyzer, the analyzer constant was verified well within required accuracy.

The energy-per-unit-charge resolution (Δ) for the analyzer is given by:

$$\Delta = \sec 2\alpha\left(\sin^2\alpha + \frac{s}{L}\cos^2\alpha\right)$$

where s is the width of the input and output slits and α is the beam incident angle measured with respect to the 45° direction from the normal. For α less than approximately 10°, Δ can be given with sufficient accuracy by:

$$\Delta = \alpha^2 + \frac{s}{L}$$

In the test model, s = 0.25 inch, a rather large slit opening, and α was negligible thus giving a resolution Δ of 6 percent.

The velocity tuner was designed to detect the hydrogen component of the solar wind, adjusting the tuner voltage until a maximum hydrogen ion current could be detected at the output slit. This tuner voltage would then provide the reference for selecting the spectrograph voltages.

2.8 SPECTROGRAPH TUNING CRITERIA

Given an incident ion energy per unit charge, U_o, the electric sector voltage V_e for 0.110 inch plates separation will be

$$V_e = \frac{U_o}{11.9}$$

wherein V_e is applied across the sector plates with a precise center-tap to ground.

For focusing at the film plane, the energy W of the ion beam entering the magnetic sector must be

$$W \sim \frac{k}{M/Z}$$

which is sufficiently close approximation for rough tuning; however, it is not exact because the magnet field is inhomogeneous and the exact expression pertains to a homogeneous field. In the expression, k is the magnet constant and M/Z is the mass/charge number. The magnet constant for a homogeneous field is calculated by

$$k_{homo} = \left(\frac{B\ r_m}{4470}\right)^2$$

where r_m = 10 cm is the central path radius of curvature. Therefore, the high intensity inhomogeneous magnet, B = 2860 gauss along the central path, has the approximate value, k = 41.

For the 1830 gauss magnet used in the present instrument, k = 16.31 was found experimentally (in close agreement with the design value of 15), therefore,

$$W \sim \frac{16.31}{M/Z} \quad \text{(kilovolt)}$$

Also,

$$W = U_o + V_a$$

where, V_a is the accelerator voltage. Then

$$V_a \sim \frac{16.31}{M/Z} - U_o$$

The voltage V_a can be varied slightly to shift the image position along the film plane.

For optimum image quality it has been experimentally determined that $V_a = 0.72\ U_o$. Combining this with the previous equations renders the following tuning criteria for a given mass/charge number:

$$U_o = \frac{9.50}{M/Z} \quad \text{(kilovolt)}$$

$$V_e = \frac{0.798}{M/Z} \quad \text{(kilovolt)}$$

$$V_a = \frac{6.80}{M/Z} \quad \text{(kilovolt)}$$

SECTION 3

DUAL QUADRANT SOLAR WIND ATTITUDE DETECTION SYSTEM

The purpose of the Solar Wind Attitude Detection System (Solar Wind Direction Indicator) is to display on a suitable device the orientation of the spacecraft in pitch and roll angles relative to the direction of maximum solar wind flux.

Assuming the aperture of the spectrograph is 1 degree, it is desirable to orient the spacecraft within ±0.5 degree for both orientation angles. Additionally, the indicator is required to display the relative degree and direction when misaligned.

The instrument designed to accomplish this task consists of three major items: two flux sensors, an electronics package, and a display device. In the description of the feasibility model which follows, the input circuitry, electronics, and display will accommodate only one orientation angle since this is sufficient for the purpose of demonstration.

3.1 SYSTEM OPERATION

Detector currents induced by the incident solar wind flux are converted into proportional voltage variations by electrometer amplifiers, E_1 and E_2 as illustrated by the system block diagram, Fig. 3-1. Rezeroing circuits are included for periodic electrometer offset compensation. These voltage outputs are further conditioned to optimally drive the dual inputs of an analog divider network.

The analog divider dividend input signal is the result of a single quadrant output modified by an amplitude range factor ($-AE_1$). The divisor input signal is the result of the sum of both quadrant outputs modified by the same amplitude range factor $[-A(E_1 + E_2)]$.

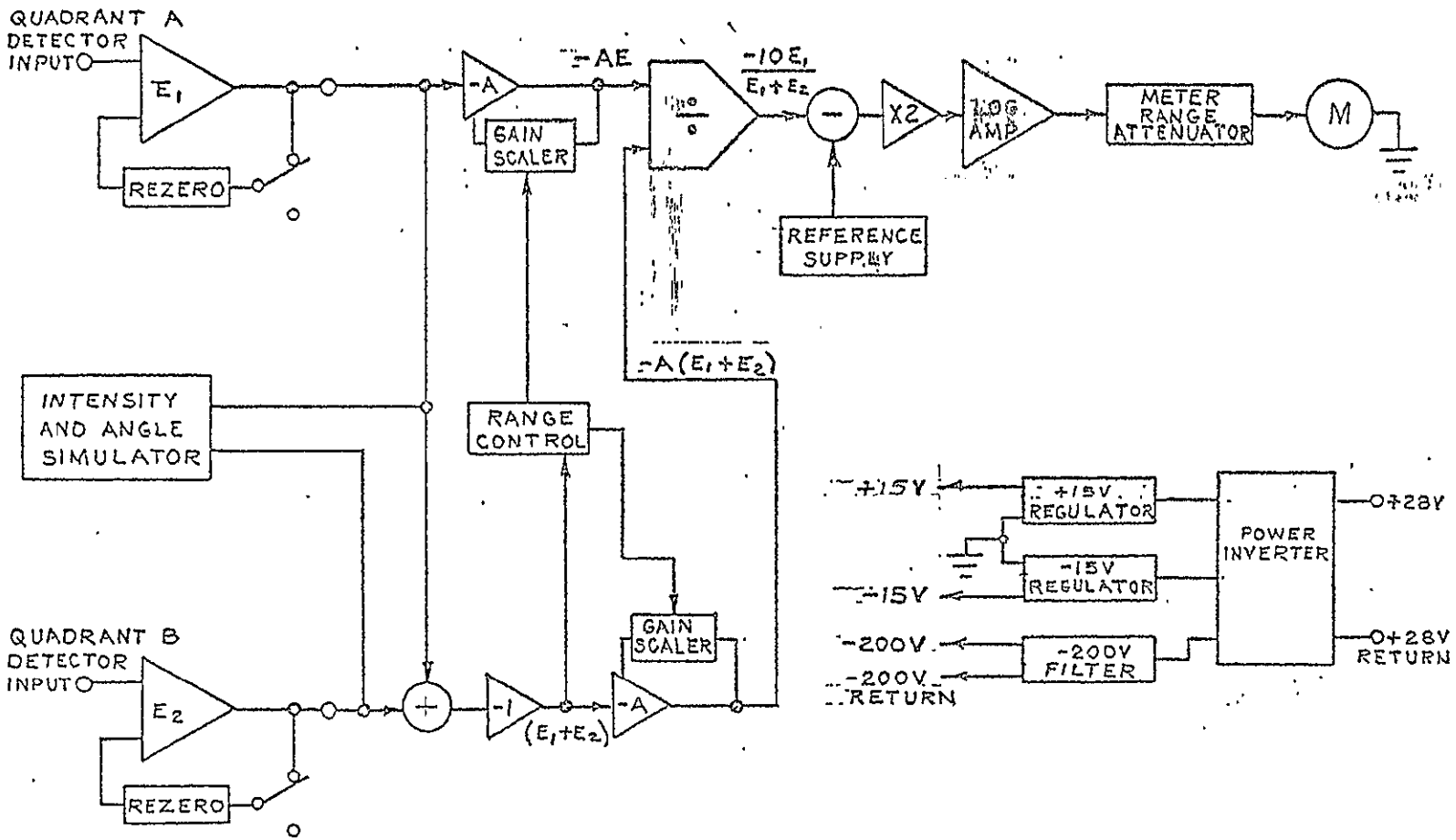

Figure 3-1. Dual Quadrant Solar Wind Direction System Block Diagram

Automatic ranging circuitry, monitoring the resulting sum of both electrometer outputs ($E_1 + E_2$), maintains high signal input levels to the analog divider with the objective of maximizing its accuracy. The resulting divider output voltage is a ratio independent of solar flux intensity variations, yet sensitive to detector attitude voltage variations.

A level shifting circuit converts the unidirectional divider output voltage levels into bidirectional levels suitable for driving the logarithmic amplifier circuit. The logarithmic amplifier provides the range compression necessary for continuously monitoring solar wind attitude displacement errors from 15° down to within 0.25°.

A zero center meter monitors the bidirectional output voltage variations of the logarithmic amplifier. It is adjusted for a maximum attitude deflection error indication of $\pm 15^{\circ}$. A range switch was included to provide scale magnification for attitude errors within $\pm 2.5^{\circ}$.

Variable intensity and attitude error simulation circuitry were included to facilitate system checkout and calibration.

Following are detailed descriptions of the individual circuits previously discussed.

QUADRANT A DETECTOR

3.2 ELECTROMETER AMPLIFIER

A Keithley Model 301 operational amplifier was selected as the basic amplifier for the electrometer. The selection was based on its low input noise and offset capabilities, as well as its high input resistance characteristics. The complete electrometer in its final form is shown in Fig. 3-2.

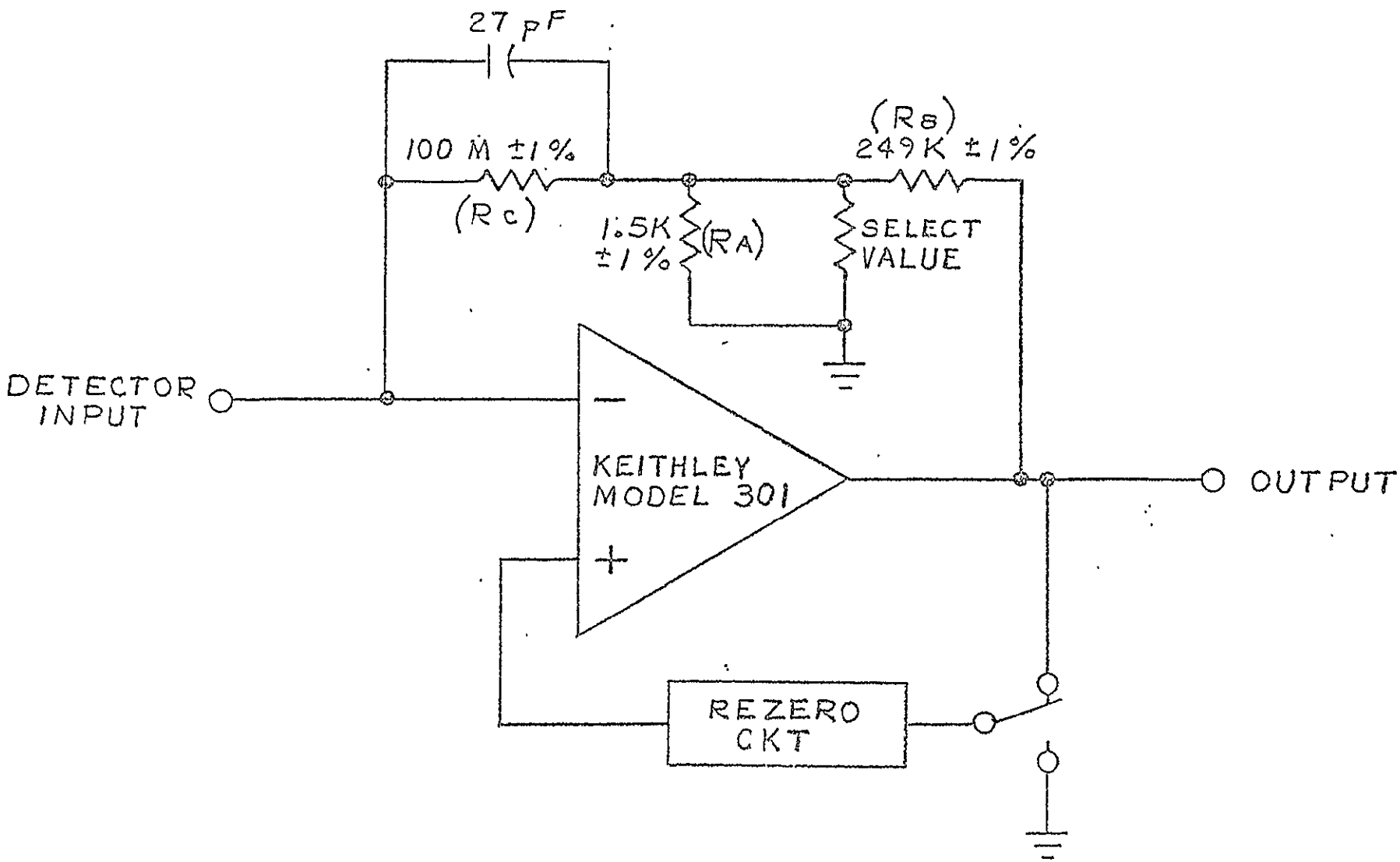

Figure 3-2. Simplified Schematic of the Electrometer Amplifier

Fractional feedback was selected to allow the use of superior temperature coefficient resistors as well as to provide a means of bandwidth control with practical values of capacitors. The output voltage of the amplifier in this configuration is related to its input current by the following equation:

$$E_o = I_{in} \frac{A\left(R_f + \frac{R_A R_B}{R_A R_B}\right)}{\left[1 + \frac{R_f}{R_{in}} + \frac{R_A R_B}{R_{in}(R_A + R_B)}\right] + \frac{A R_A}{R_A + R_B}}$$

where:

A = Amplifier open loop gain

R_{in} = Amplifier input resistance

when:

$R_{in} \gg R_A$, R_B, or R_f

$R_f \gg R_B$

$R_B \gg R_A$

$A > 50$

then:

$$E_o \approx I_{in}\left(\frac{R_B R_f}{R_A}\right)$$

An equivalent transresistance of 2.5×10^{10} ohms was selected to provide maximum amplifier output commensurate with maximum design flux density. The 100 megohm feedback resistance has a temperature

coefficient of 80 ppm/^{o}C, restricting variations in transresistance to less than 0.5 percent over the operational temperature range.

A detailed noise analysis of the electrometer was performed, resulting in the following relation for its output noise voltage:

$$E_N \approx R_B \sqrt{I_A^2 + I_B^2} \cdot \frac{R_B R_f}{R_A} \sqrt{I_S^2 + I_n^2 + I_f^2 + \left[\frac{E_n}{\left(\frac{R_f Z_s}{R_f + Z_s}\right)}\right]^2}$$

where:

I_A = Thermal noise of R_A

I_B = Thermal noise of R_B

I_f = Thermal noise of R_f

I_s = Detector noise

I_n = Amplifier input current noise

E_n = Amplifier input voltage noise

Z_s = Detector impedance

Substituting values into the above equation revealed that the dominant contribution of noise was from the amplifier input voltage noise source. This result was instrumental in determining the point of bandwidth control for the electrometer. The measured quiescent output noise of the electrometer was less than 5 mV rms, in agreement with the analytic value determined from the above relation.

The electrometer bandwidth was limited to within 50 Hz as a compromise between system dynamic response and noise. The gain and phase characteristics were empirically measured resulting in the curves of Figs. 3-3 and 3-4. The stability of the electrometer is reflected by its 110 degree phase margin.

3.3 REZERO CIRCUIT

Electrometer offsets due to drift are compensated for by the rezero circuit of Fig. 3-5. The rezero circuit is basically a sample and hold circuit consisting of a high quality, low leakage 10 μfd mylar capacitor and a low gate leakage insulated gate field effect transistor.

The capacitor initially charges up to the electrometer output offset level and is inverted, when switched to the rezero position, transferring the inverse offset potential to the input of a source follower circuit. The source follower output is attenuated by an amount equal to the fractional feedback ratio and applied to the positive input of the electrometer.

Although the rezero circuit is capable of rezeroing the electrometer output to within five millivolts, and retaining this offset for over an hour, the amplifier offset should be sampled approximately every 20 minutes in order to insure low drift offset levels.

3.4 RANGE CONTROL

The accuracy of the analog divider module deteriorates rapidly with input voltage levels below 4 volts. Increasing the system gain at low flux levels reduces these inaccuracies. The range control circuit detects and increases system gain when flux levels drop below a prescribed value.

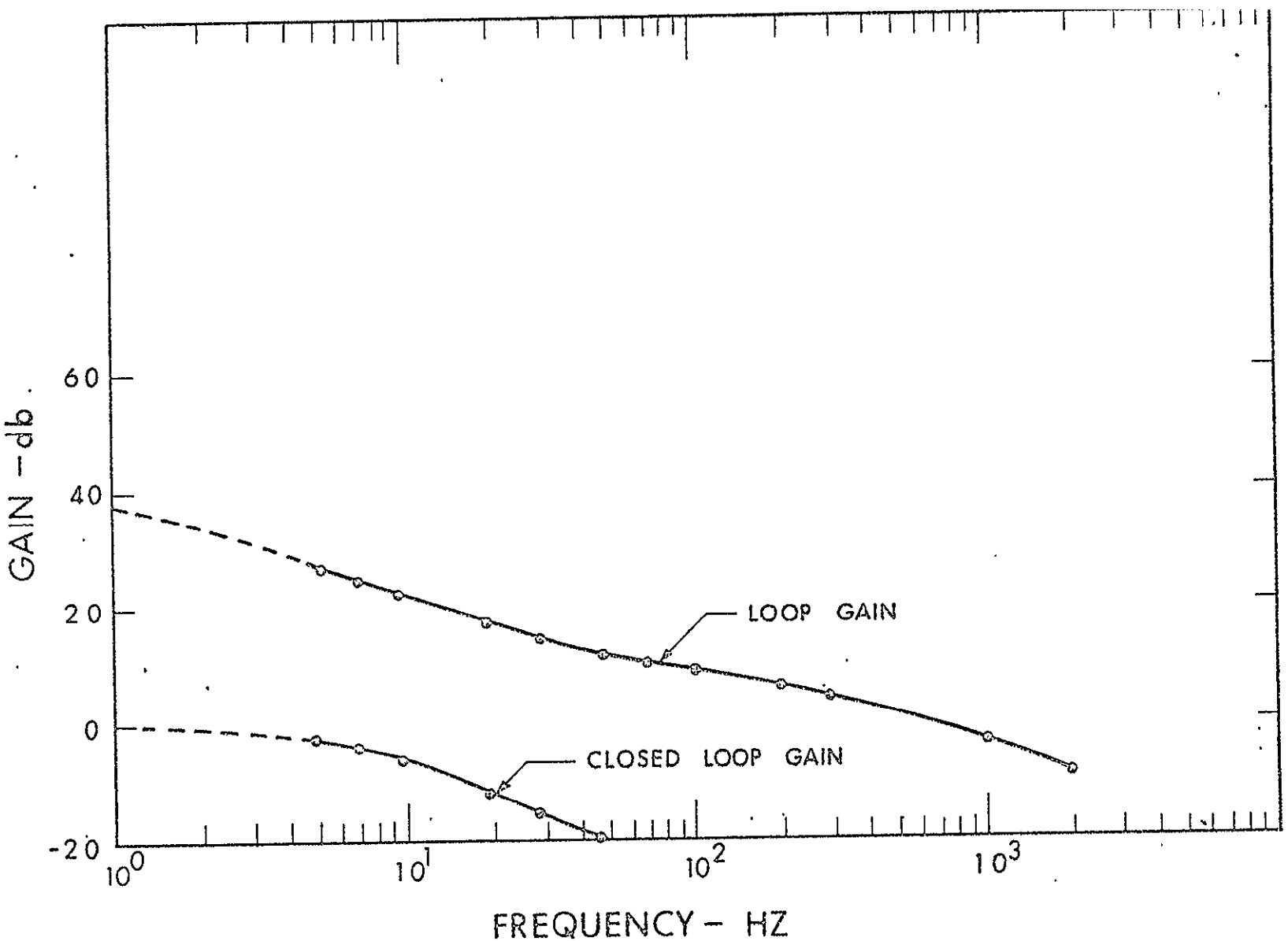

Figure 3-3. Electrometer Gain Controls

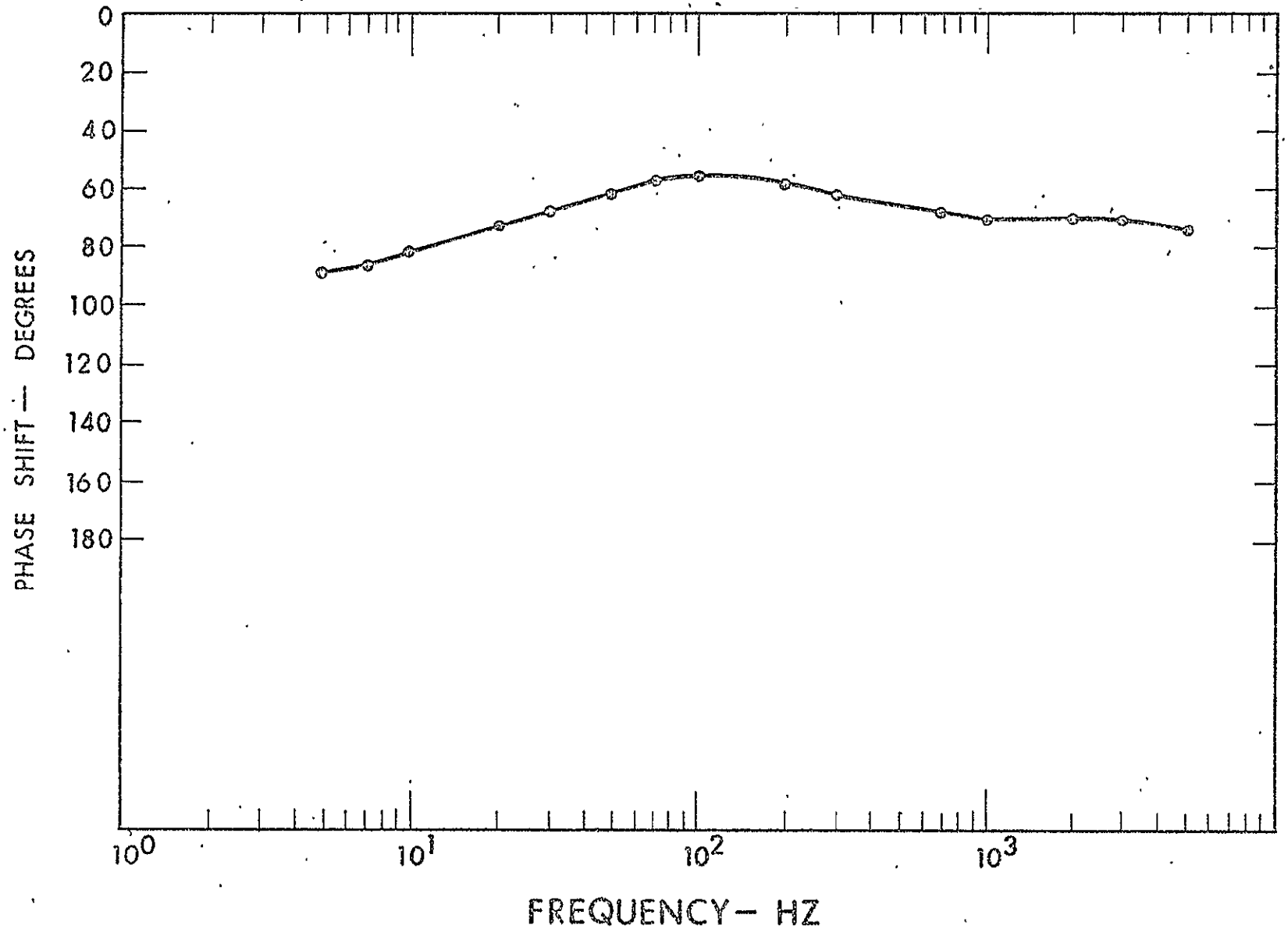

Figure 3-4. Electrometer Phase Characteristics

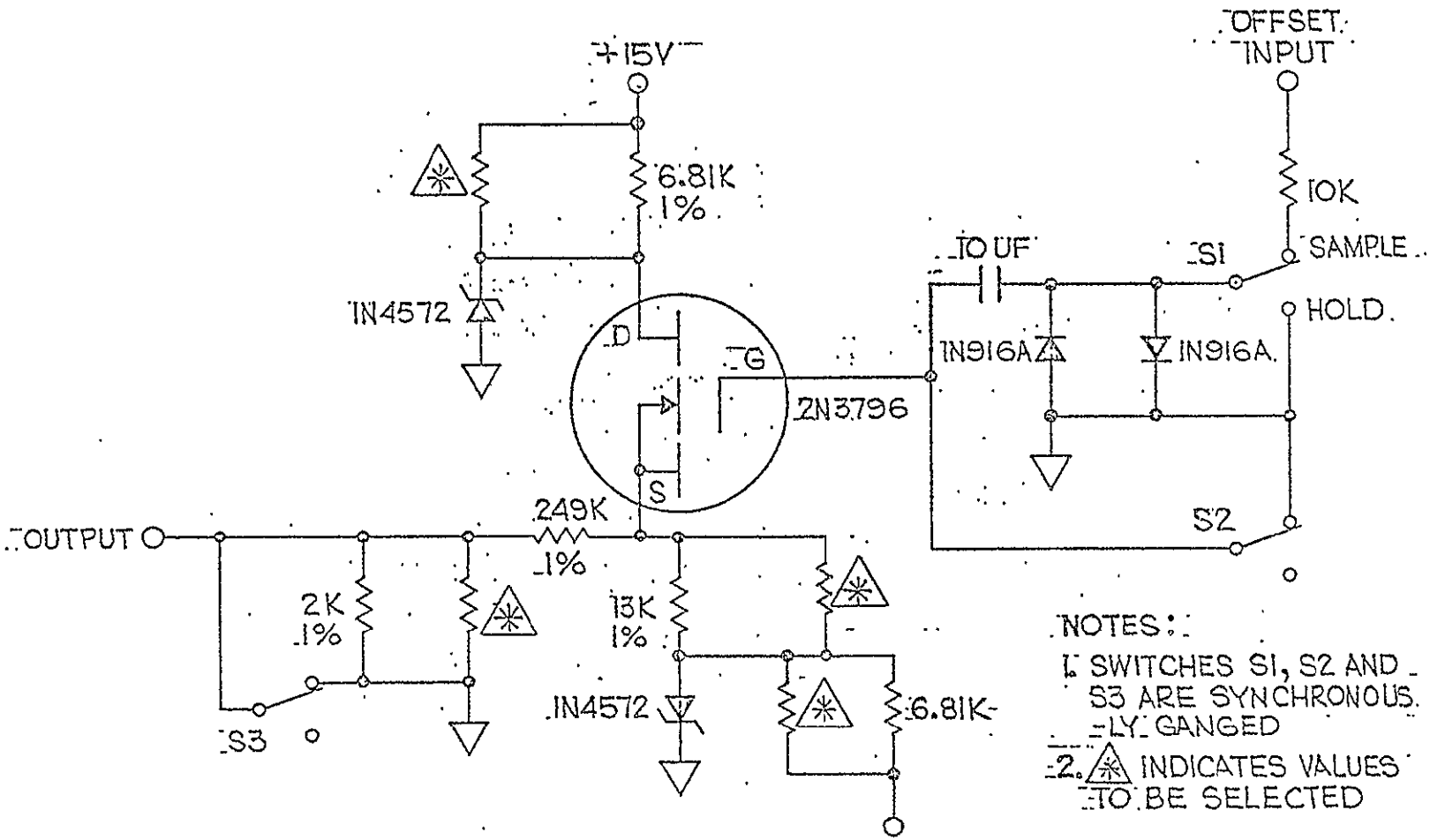

Figure 3-5. Rezero Circuit

The range control circuit shown in Fig. 3-6 consists of a voltage level comparator driving a voltage translator circuit. The comparator, a differential amplifier, was designed with approximately one volt of transition hysterisis to provide range overlap, reducing transition instability. The upper level transition point occurs at 5.5 volts, equivalent to an intensity level at approximately $2.75 \times 10^8 \frac{\text{ions}}{\text{cm}^2\text{-sec}}$. The lower level transition point occurs at 4.5 volts, equivalent to an intensity level of approximately $2.25 \times 10^7 \frac{\text{ions}}{\text{cm}^2\text{-sec}}$. This accommodates the expected range of hydrogen ion flux intensities in the solar wind.

The voltage translator circuit converts the comparator 4 volt logic level output into voltage excursions capable of controlling field effect transistor switches. These switches are used to alter the resistive feedback values of signal chain amplifiers.

3.5 LOG AMPLIFIER

The alignment resolving capability of the system is enhanced by the logarithmic amplifier. Its logarithmic transfer characteristic was specifically designed to increase system sensitivity for input voltage levels approaching zero, with zero voltage indicative of perfect alignment.

The log amplifier of Fig. 3-7 is basically an operational amplifier with its feedback resistance shunted by bidirectional transistor logarithmic elements Q_{L1} and Q_{L2}. These logarithmic elements are designed to operate at zero collector to base voltage, effectively eliminating the collector to base leakage components. The bias elements, Q_{B1} and Q_{B2}, keep the logarithmic element operational by providing bias current through isolation amplifiers A_B.

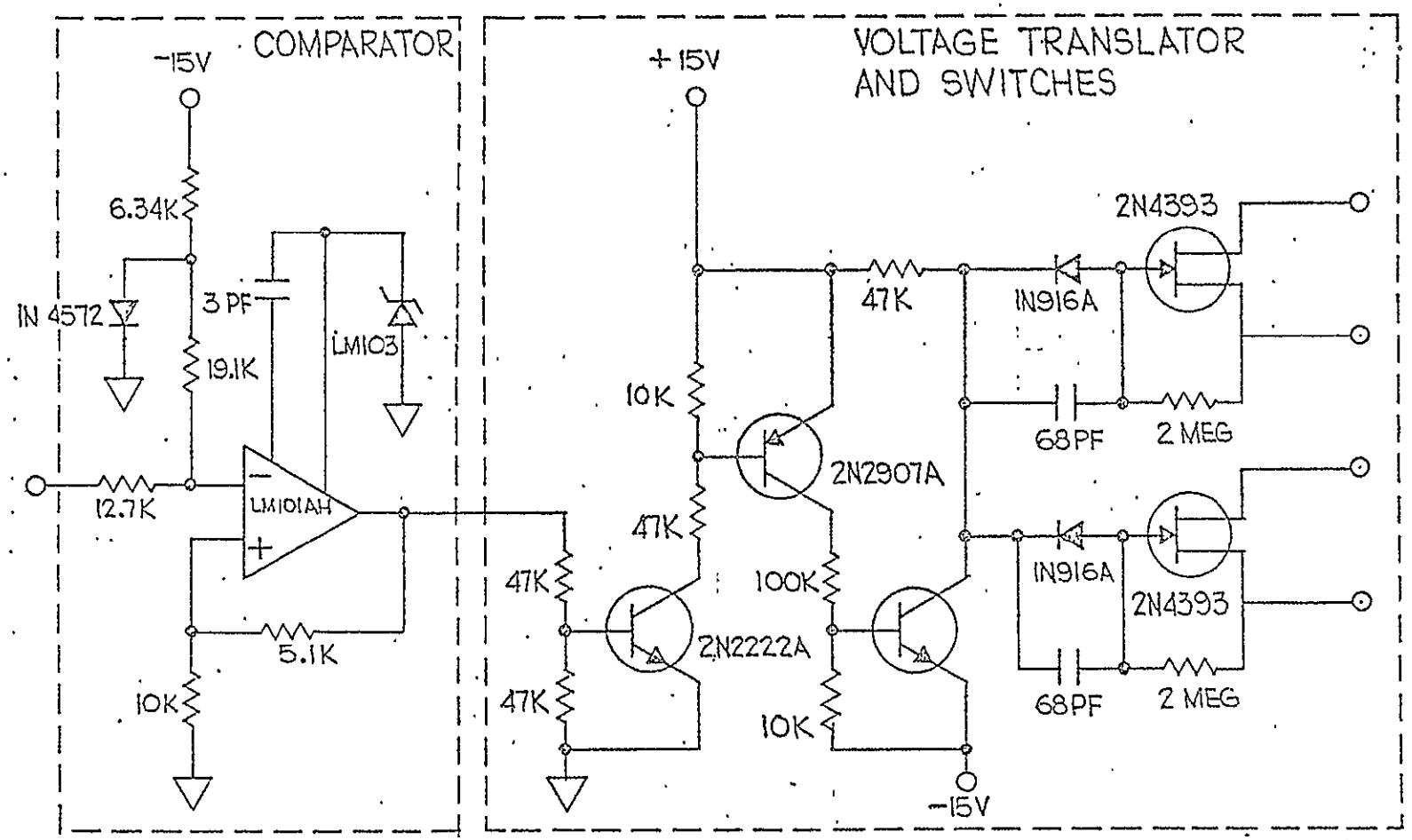

Figure 3-6. Simplified Schematic of the Range Control Circuit

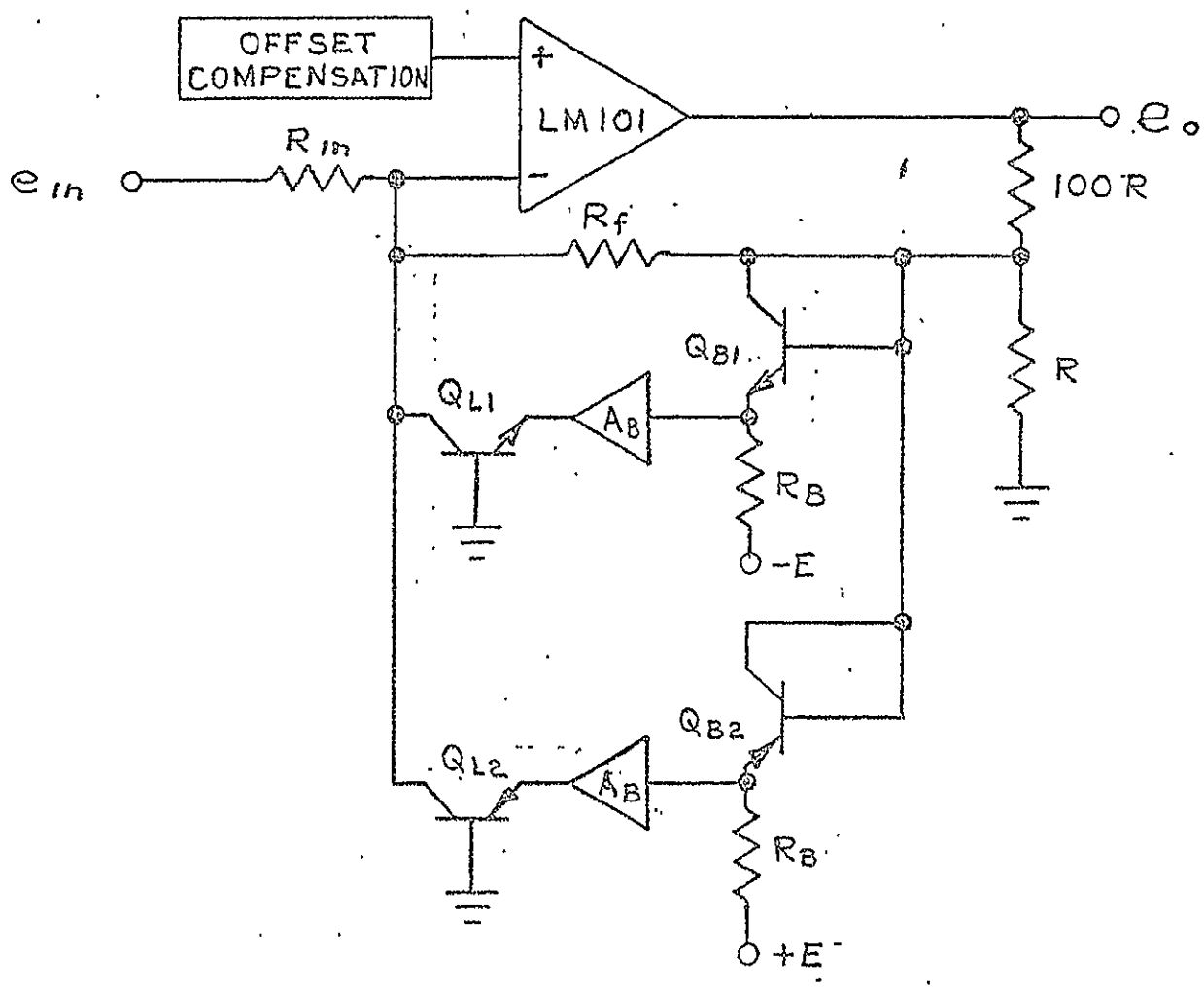

Figure 3-7. Simplified Schematic of the Logarithmic Amplifier

The log amplifier input voltage is related to its output voltage by the following relation:

$$e_{in} = \frac{-R_{in}}{R_f} \left[0.01\ e_o + 2I_B\ R_f\ \text{Sinh}\left(\frac{116\ e_o}{R}\right)\right]$$

where:

I_B = Current in bias element Q_B

T = Absolute temperature ^oK

The resulting empirical transfer characteristic is given in Fig. 3-8.

3.6 INTENSITY AND ANGLE SIMULATOR

Verification of system calibration and operability is provided by the intensity and angle simulator. It is designed to generate voltage levels equivalent to flux intensities up to $5 \times 10^8 \frac{\text{ions}}{\text{cm}^2\text{-sec}}$ and to simulate angular deviations up to ±15 degrees.

A simplified schematic diagram of the simulator is shown in Fig. 3-9. Intensity voltages derived from a ten-turn potentiometer are transferred to a summing amplifier where they are combined with an inverse fraction of their value, resulting in the differential value of the combination. The resulting outputs at E_1 and E_2 are therefore always complementary fractions of the intensity voltage. Unequal fractional output values represent an angular deviation, capable of continuous adjustment up to 10 degrees. A deviation of 15 degrees must be switched in. The phase inverting switch at the output enables the simulation of maximum intensity at either detector.

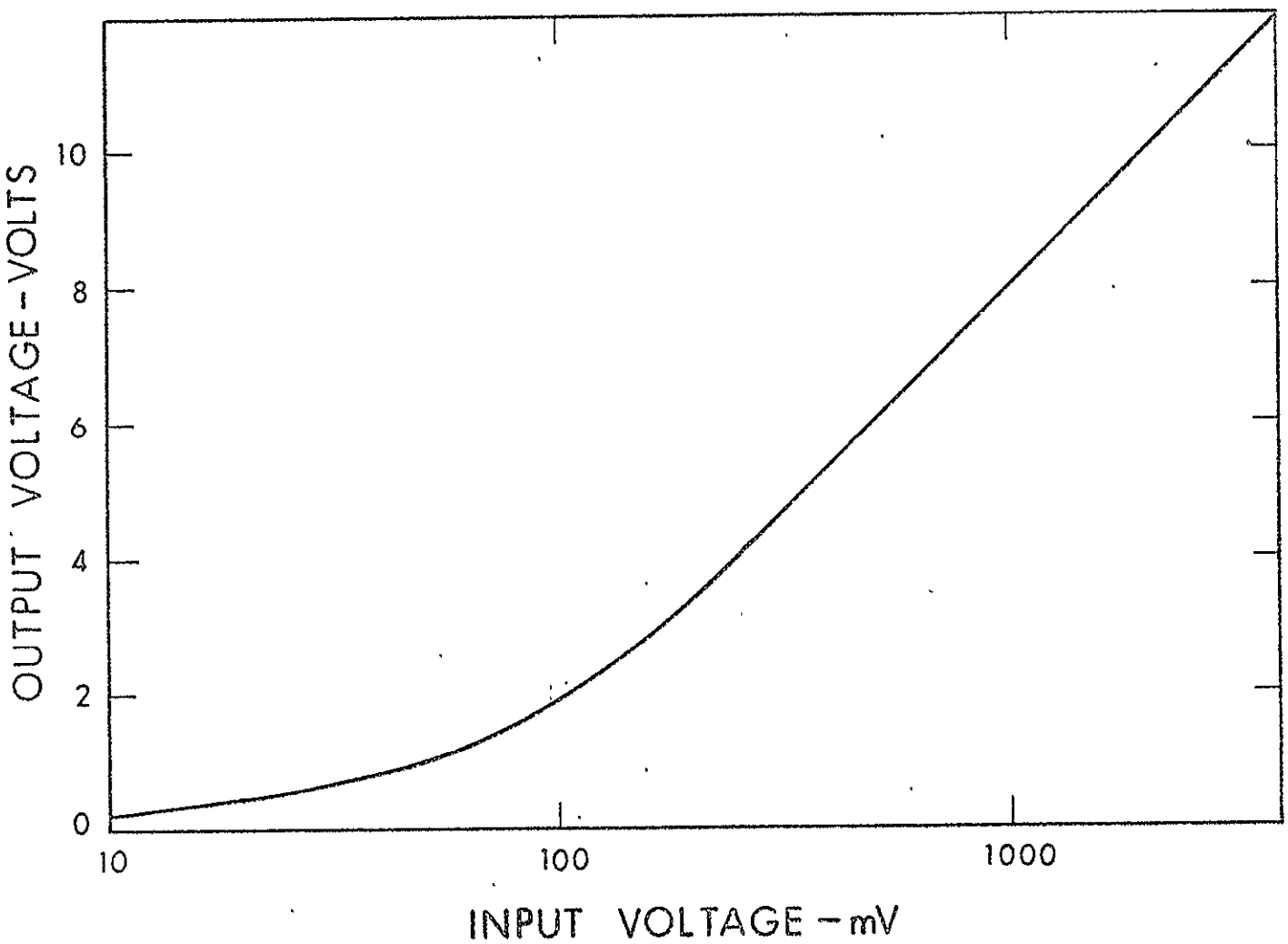

Figure 3-8. Logarithmic Amplifier, Experimental Data

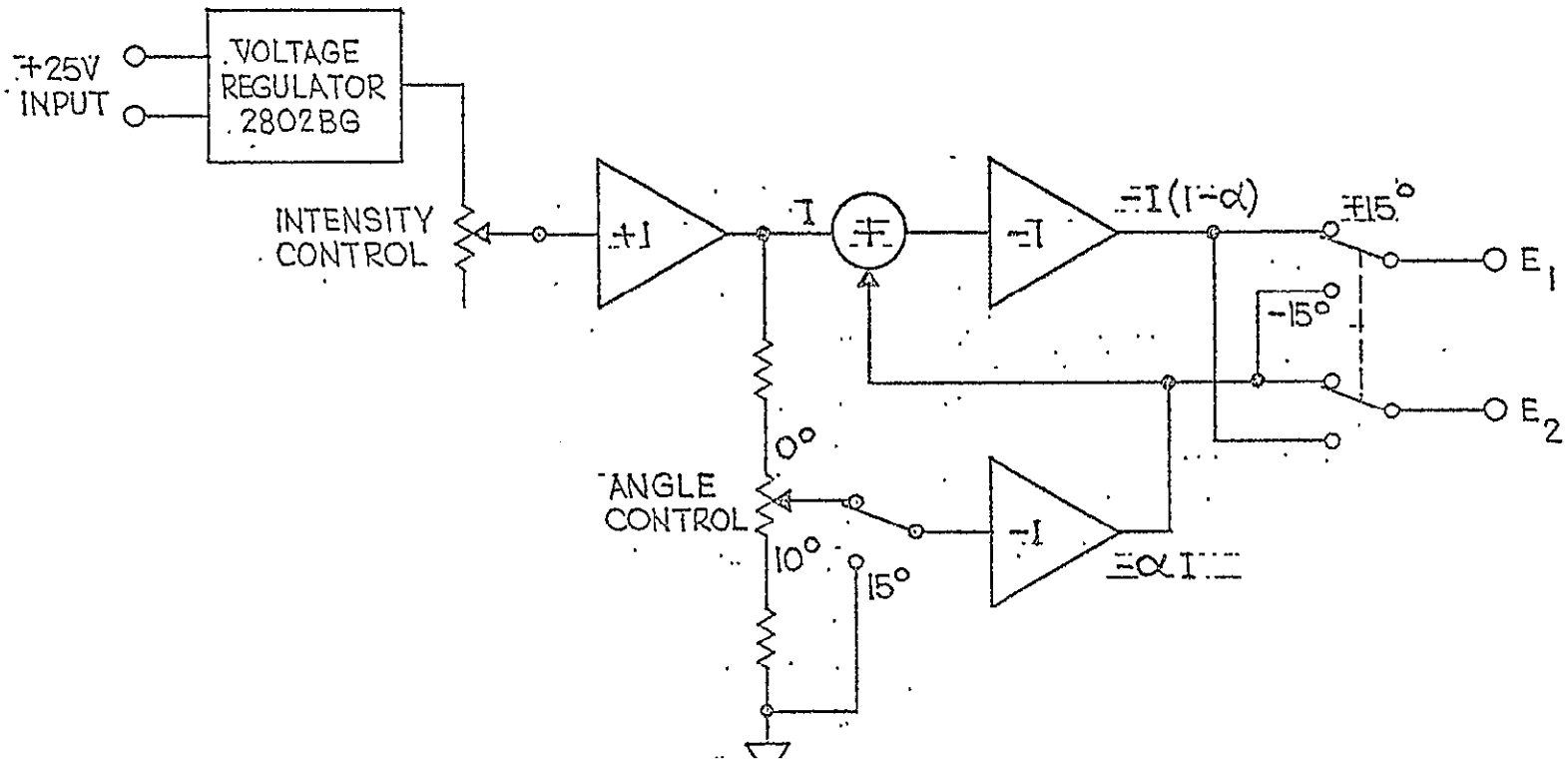

Figure 3-9. Simplified Schematic of the Intensity and Angle Simulator

The simulator outputs correspond to expected electrometer amplifier outputs and therefore the electrometer amplifier outputs are not included in the test. The application of simulator voltages to the system is performed by a switch on the front panel.

3.7 SYSTEM POWER SUPPLY

The system power supply is basically a saturable transformer base driven dc converter with a nonsaturating dual secondary output transformer. A bridge rectified, capacitance filtered, center-tapped secondary provides the drive for the positive and negative 15 volt regulators. A voltage doubler on the remaining secondary winding produces a 200 volt retarding screen potential which will be used to prevent solar wind electrons from reaching the input signal collectors.

The ±15 volt outputs are capable of supplying 100 mA with a load regulation better than 0.05 percent. Figure 3-10 is a simplified schematic of the system power supply.

3.8 SUMMARY

Figure 3-11 shows the detailed schematic of the dual quadrant solar wind attitude detection system. Figure 3-12 is a photograph of the instrument. This feasibility model was developed using commercially available components. Although a system accuracy within 5 percent resulted, an instrument with a rating better than 2 percent would be possible with selected and flight-tested components.

Improvements such as replacing the 1 percent analog divider module with one rated at 0.1 percent or better and the addition of at least one more amplitude range level, insuring optimum analog divider accuracy, could be incorporated.

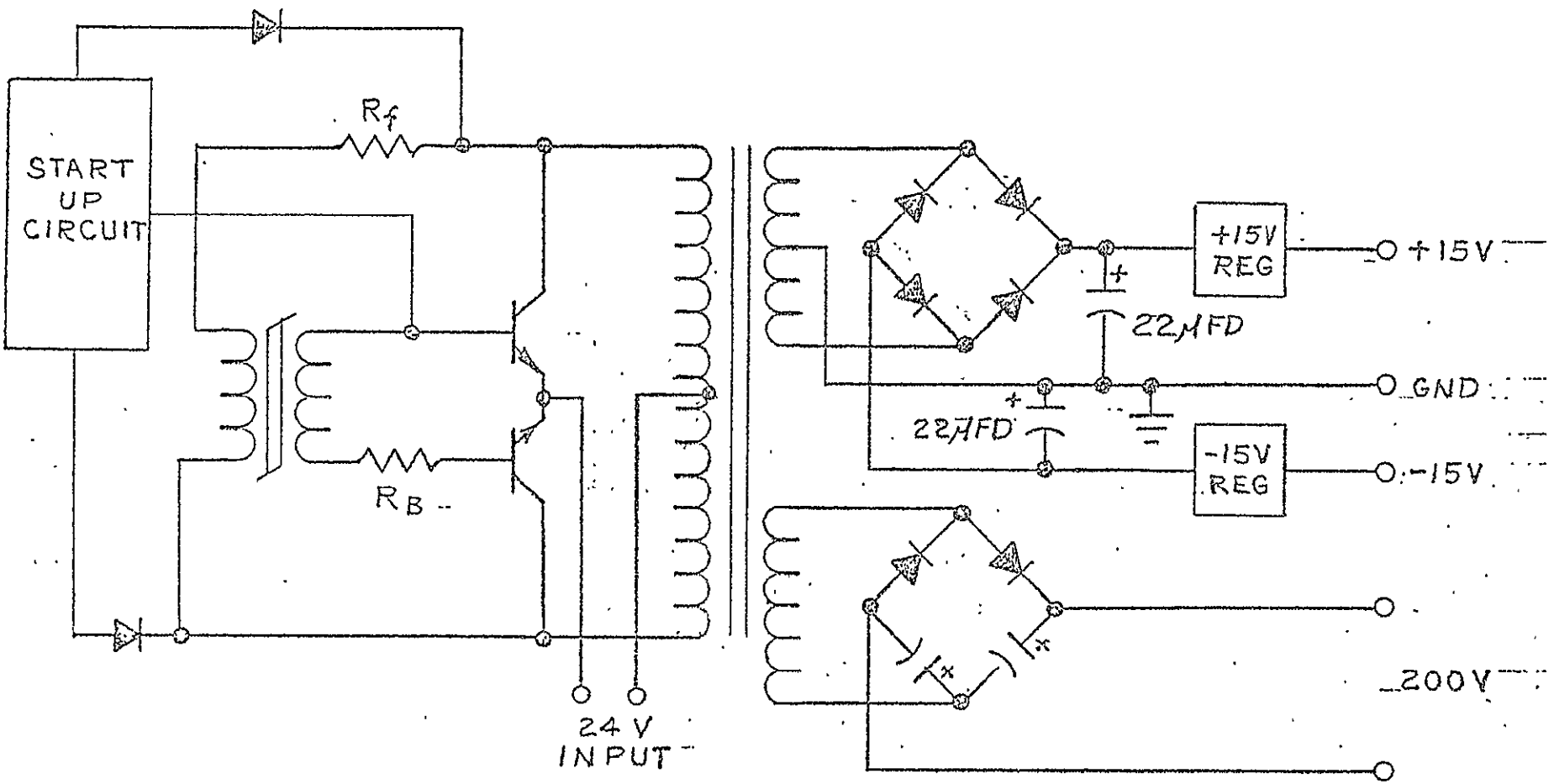

Figure 3-10. Simplified Schematic of the System Power Supply

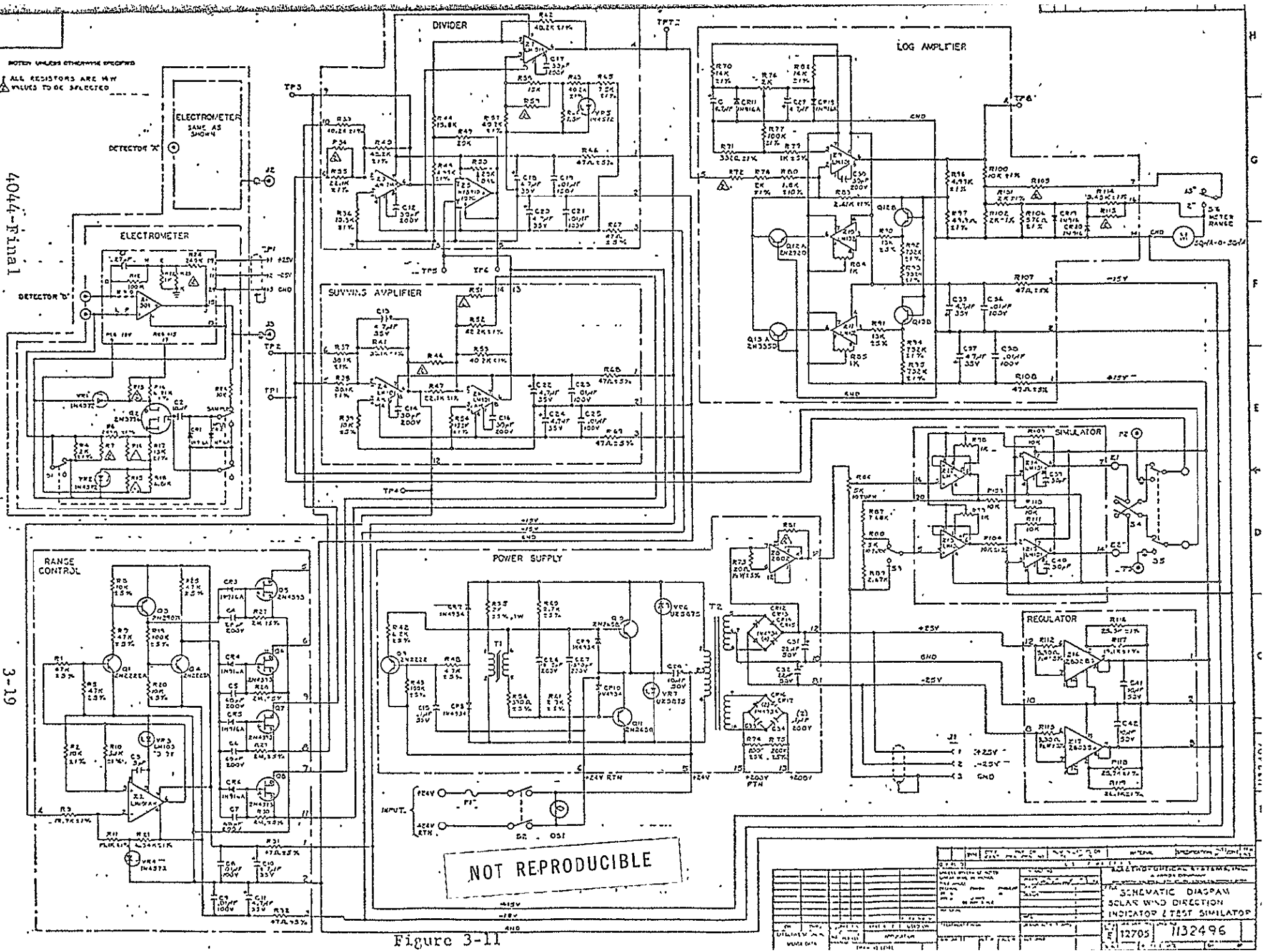

4044-Final

3-19

Figure 3-11

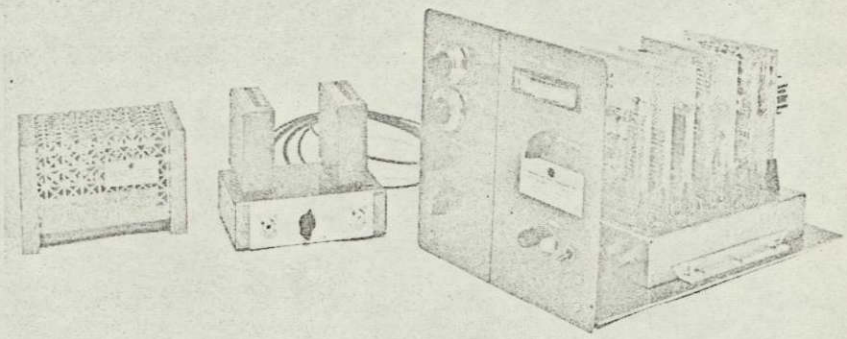

57070

Figure 3-12a. Solar Wind Direction Indicator

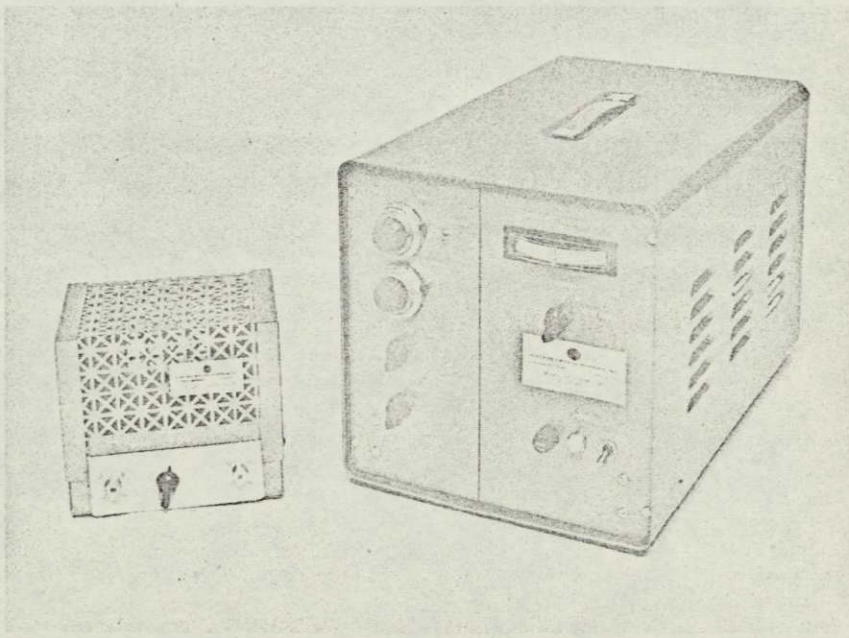

57069

Figure 3-12b. Solar Wind Direction Indicator

Temperature compensation circuitry would be included in the logarithmic amplifier and rezeroing circuits. If necessary, the electrometer output noise level could be reduced further by almost a factor of two within the same design limitations.

The size and weight of a flight instrument would be minimized with the use of integrated circuits wherever possible. Critical circuits, such as the electrometer amplifiers, the logarithmic amplifier, and, if necessary, the analog divider circuit would be designed with high quality selected discrete components.

The variable intensity and attitude error simulation circuitry could become part of the ground support equipment allowing further weight and size reduction of the flight instrument.

The meter selected for the feasibility model was for demonstration purposes only and would be replaced by a high quality dual pointer flight tested unit.

The ion flux collector for the direction indicator has been designed. This unit (two required for the flight instrument) will be wedge-shaped with a 30^{o} angle and with each wing of the wedge consisting of a two-grid-and-plate assembly. The grid arrangement will retard solar wind electrons and also contain photon and ion-induced secondary emission electron currents within the collector such that these currents will not appear as a signal component. This is accomplished by arranging the potentials wherein the center grid is biased negative with respect to the plate and input grid, thereby confining the non-signal currents to closed grid-grid and grid-plate loops. The additional 200 volt output from the instrument power supply will be used as the source of retarding potential.

An ion flux collector used to test the instrument in the facility is shown in Fig. 3-13. Excellent correlation between angle simulation and orientations with respect to the ion beam was obtained.

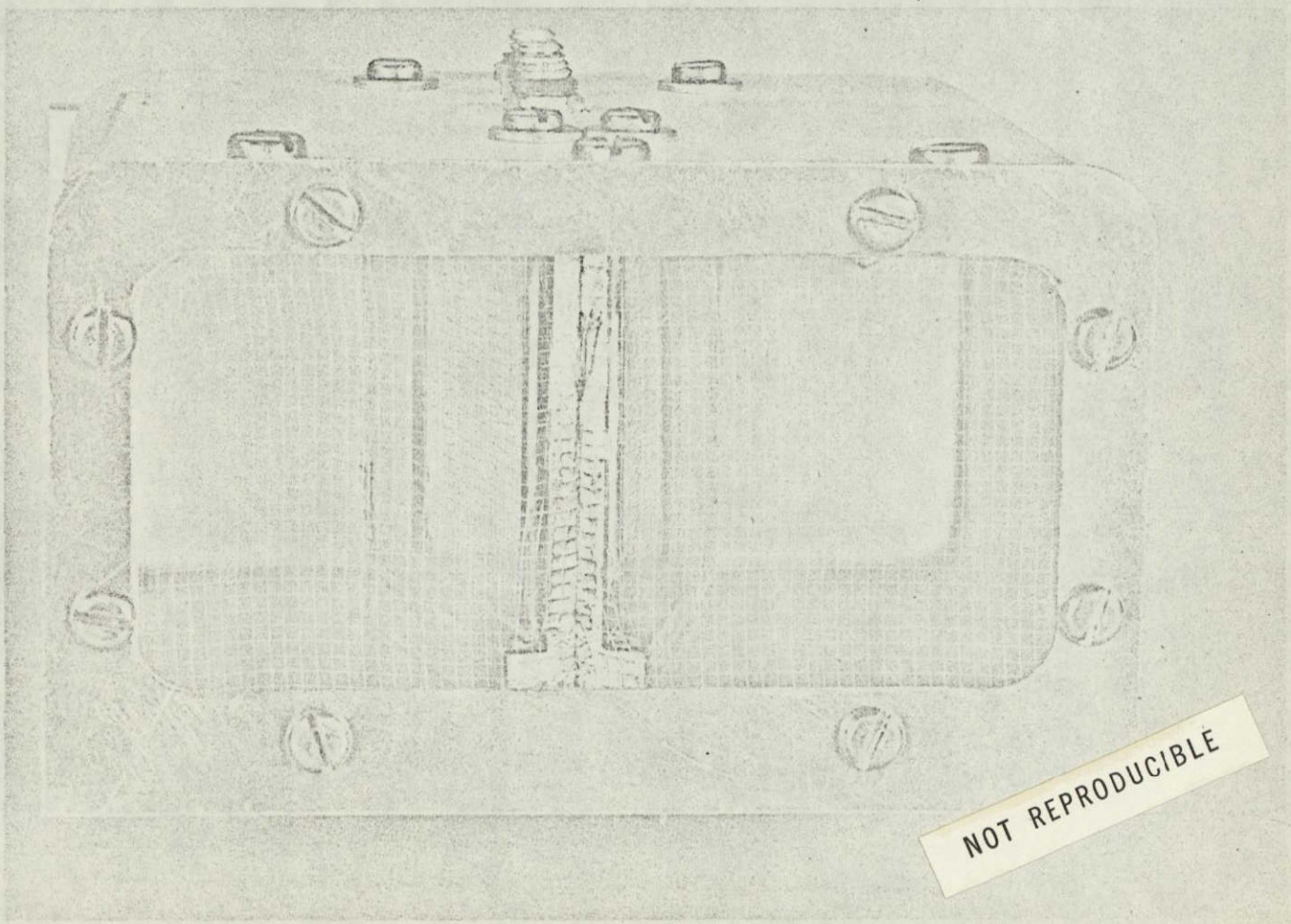

Figure 3-13. Ion Flux Collector Used in Testing Solar Wind Indicator

SECTION 4

TEST FACILITY

4.1 ION SOURCE

Figure 4-1 shows a schematic of the electron bombardment ion source and associated electronics. This source was adapted from a standard bombardment ion engine. An important change required the replacement of the beam forming electrode by a plate with very small orifices in order to reduce ion current and restrict gas flow from the source. Also the extractor electrode was modified. Collimation is accomplished by passing the ion beam through an electrically isolated rectangular-shaped metal liner which is placed co-axially with the source. The location of the liner is shown in Fig. 4-2.

The ion source electronics consists of the following power supplies:

0 to 15V, 0 to 30A	(cathode heater)
0 to 36V, 0 to 5A	(magnet)
0 to 60V, 0 to 1A	(arc)
0 to 300V, 0 to 0.15A	(accelerator)

The ion energy supply is an Electronic Research Associates Model TH5K-15LM, which has a variable output of 0 to 5 kV, 0 to 0.015A with a line and load regulation of 0.01 percent or 50 mV, whichever is greater. This potential is monitored by a John Fluke Differential Voltmeter with an accuracy of 0.02 percent.

All of the ion source electronics except the ion energy supply and differential voltmeter are located in a console at the source end of

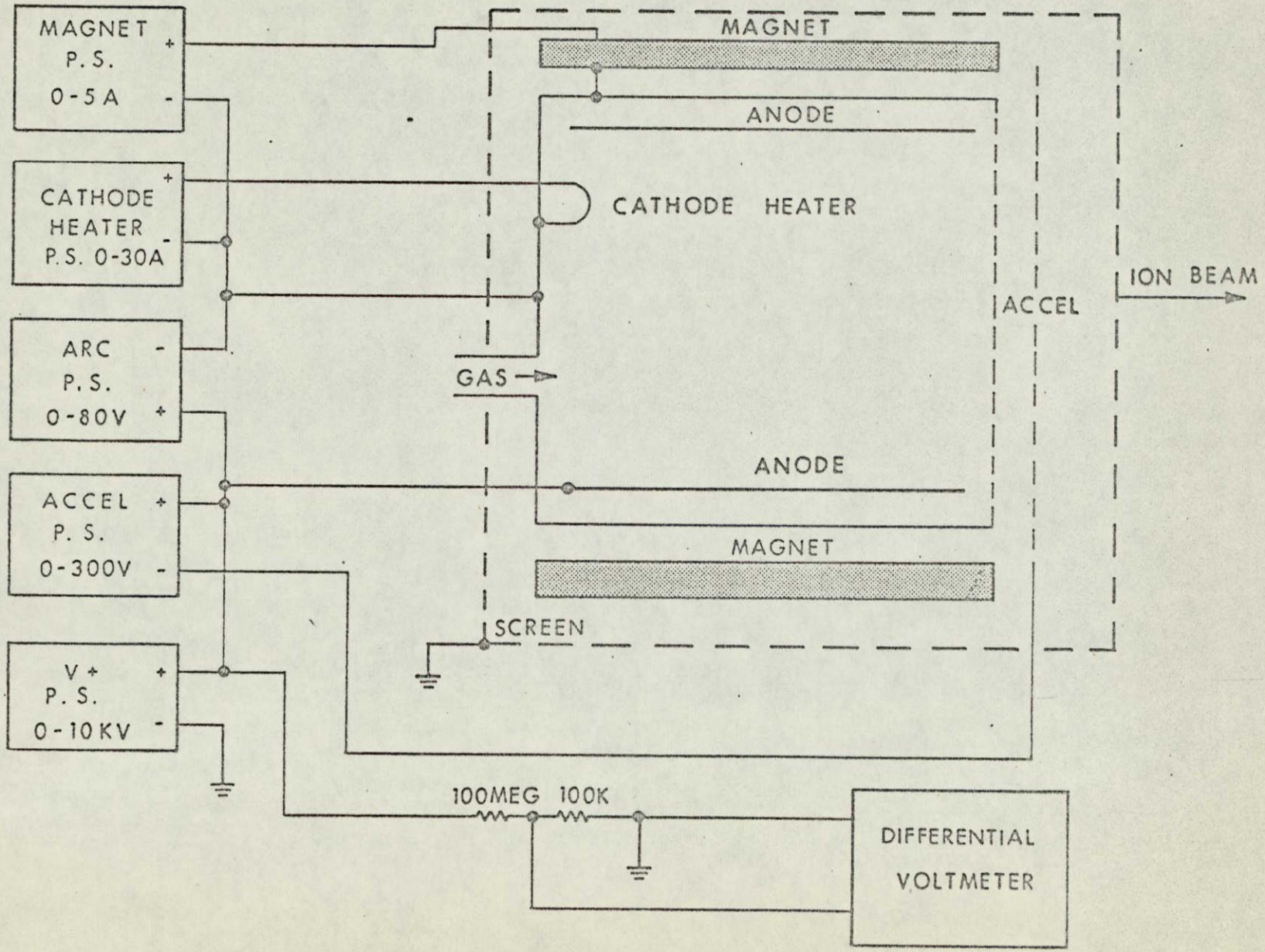

Figure 4-1. Electron Bombardment Ion Source Schematic

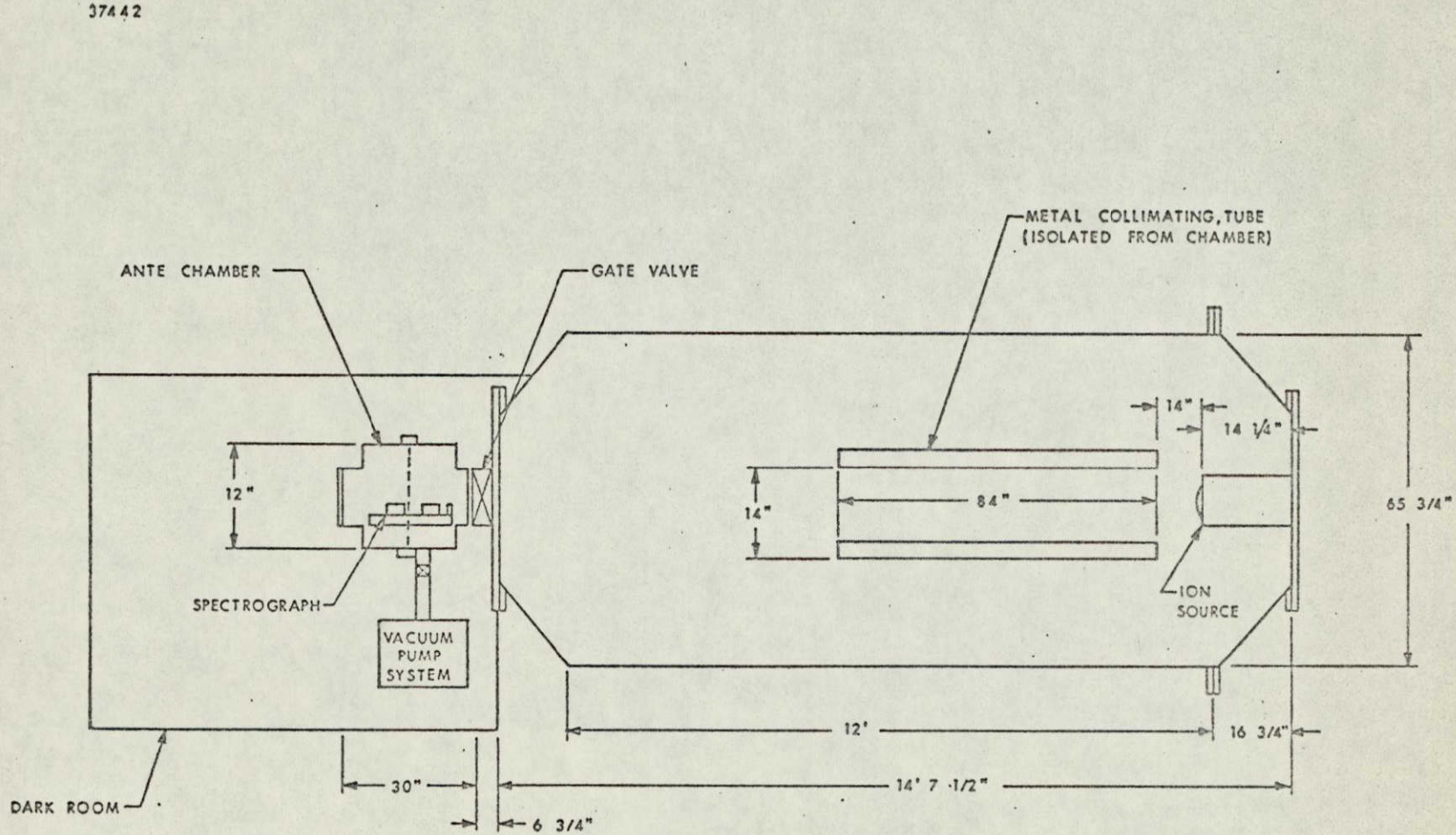

Figure 4-2. Schematic of Spectrograph Test Facility

the 5' x 12' vacuum chamber. The ion energy supply and monitoring voltmeter are located in the dark room for easy access during experiments.

Typical operating parameters for a helium ion current density of 2×10^{-13} A/cm^2 at the far end of the chamber are:

cathode heater	- 20.5A
magnet	- 0.8A
arc current	- 25 microamperes
arc voltage	- 60V
accelerator	- 100V
Δp (due to gas flow)	- 7×10^{-7} torr

4.2 VACUUM SYSTEMS

The 5' x 12' chamber has six 10-inch oil diffusion pumps, each capable of a 4000 liter/second pumping speed. Operating pressures are in the 10^{-7} torr range with liquid N_2 trapping of condensibles under gas load conditions. Typical operation on two diffusion pumps with refrigeration trapping is 4.0×10^{-7} torr increasing to 1.2×10^{-6} torr with the ion source operating ($\Delta p \sim 7 \times 10^{-7}$ torr).

Figure 4-3 shows the chamber and control console. Also the ion source installation and associated electronics can be seen in this photograph. Figure 4-4 provides a view of the diffusion pumps and the dark room which houses the ante-chamber and spectrograph electronics.

The ante-chamber is a 12" x 30" horizontal cylinder attached to the end of the 5' x 12' chamber separated by a 6-inch gate valve. The ante-chamber has an independent pumping system capable of the 10^{-7} torr range. This chamber, which is used to house the spectrograph (see Figs. 4-5 and 4-6), can be repeatedly opened to atmosphere and reduced to 10^{-6} torr

57073

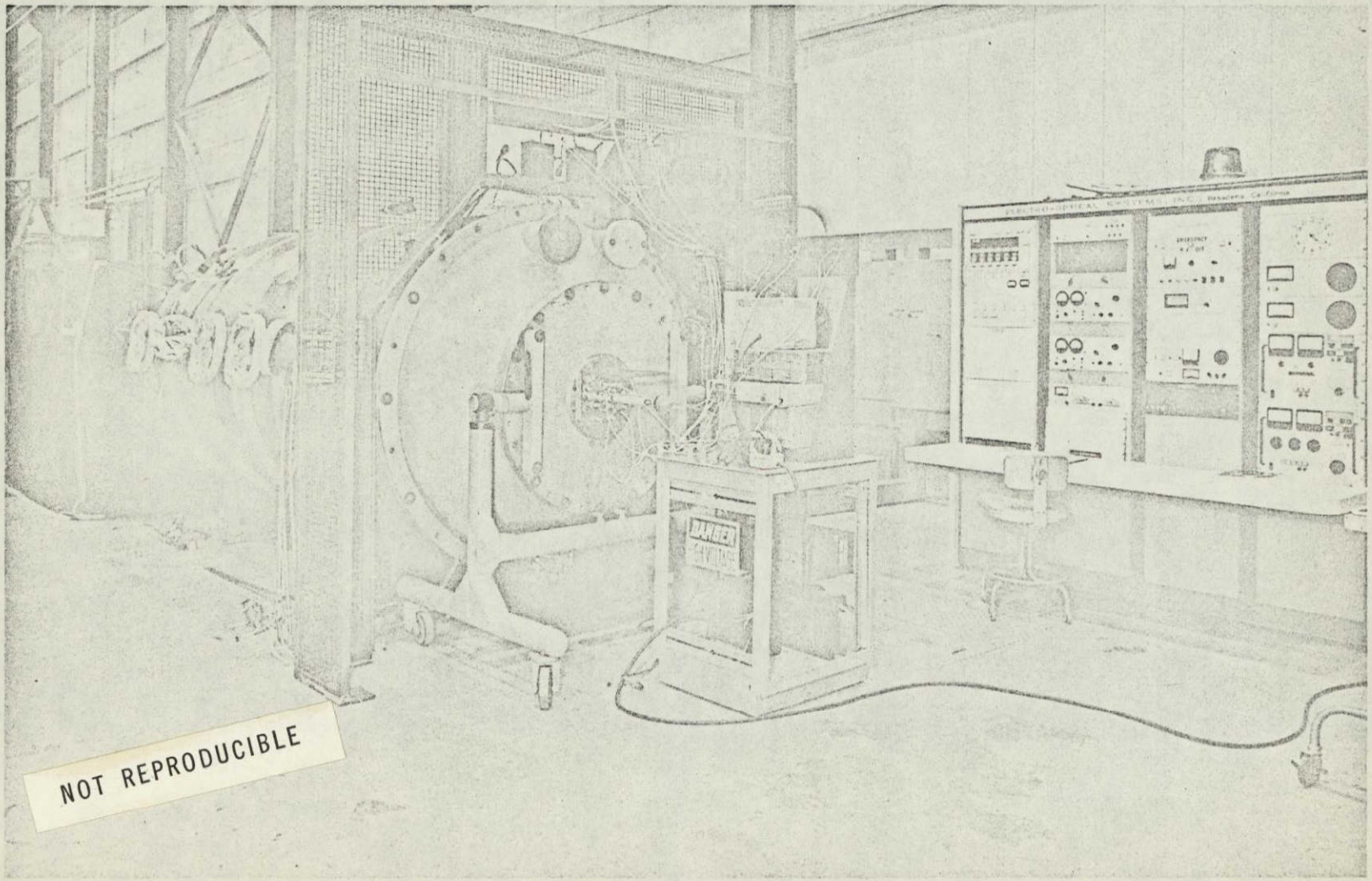

Figure 4-3. 5 foot by 12 foot Chamber and Control Console (Showing View of Ion Source Installation and Electronics)

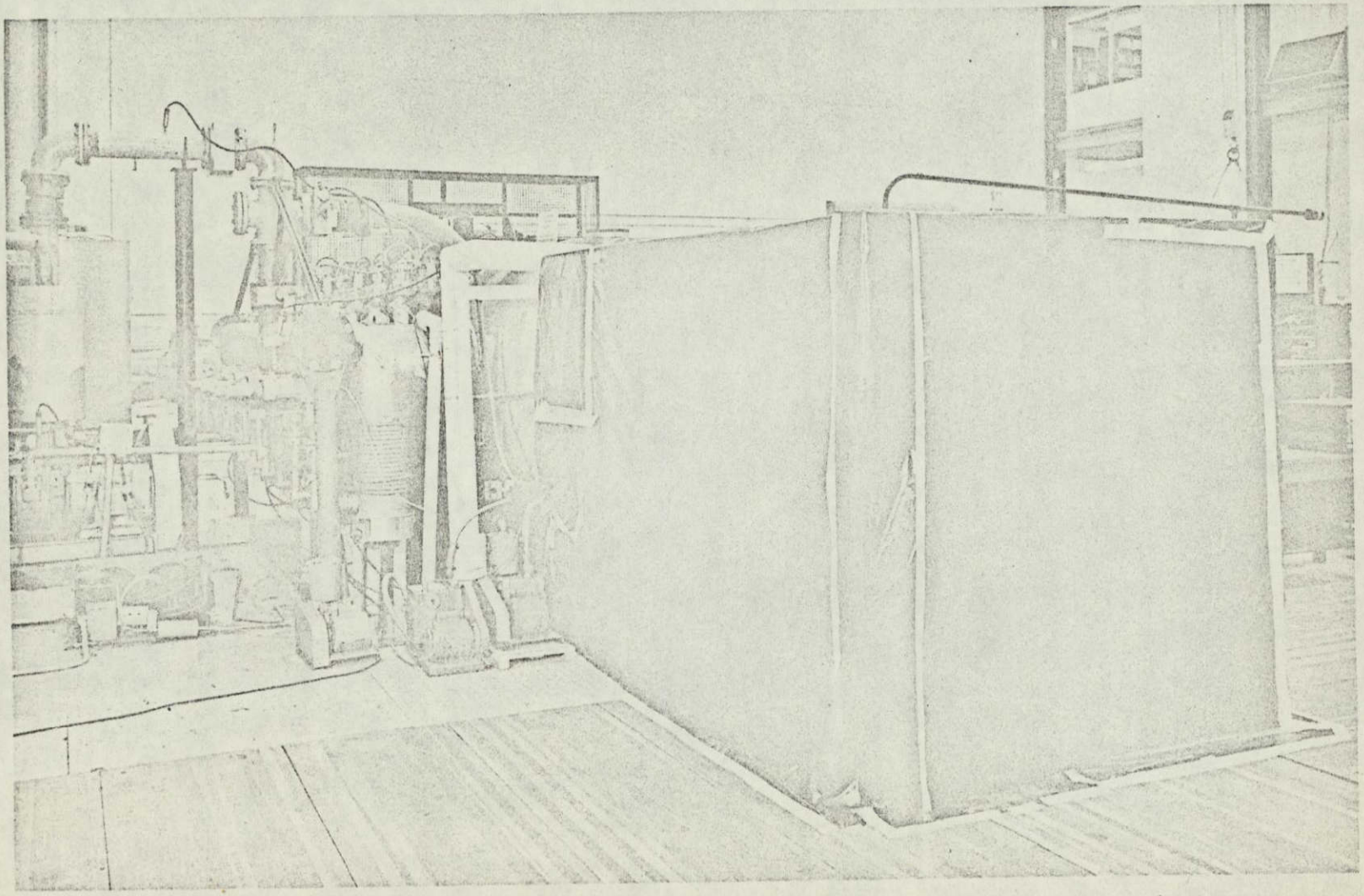

Figure 4-4. View of 5 foot by 12 foot Chamber Diffusion Pumps and the Portable Dark Room

57075

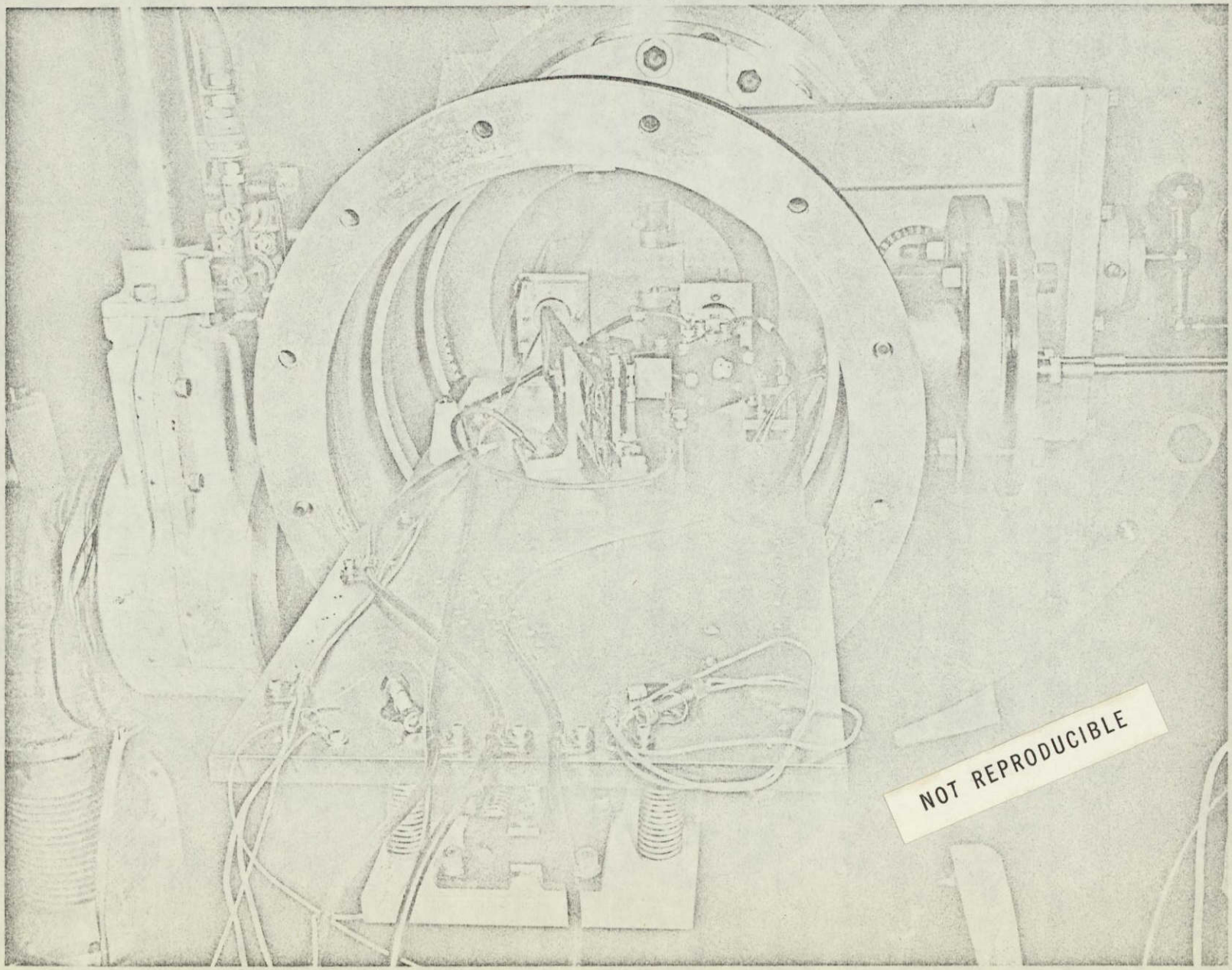

Figure 4-5. Dark Room Test Facility Showing Ante-Chamber and Spectrograph Electronics

57072

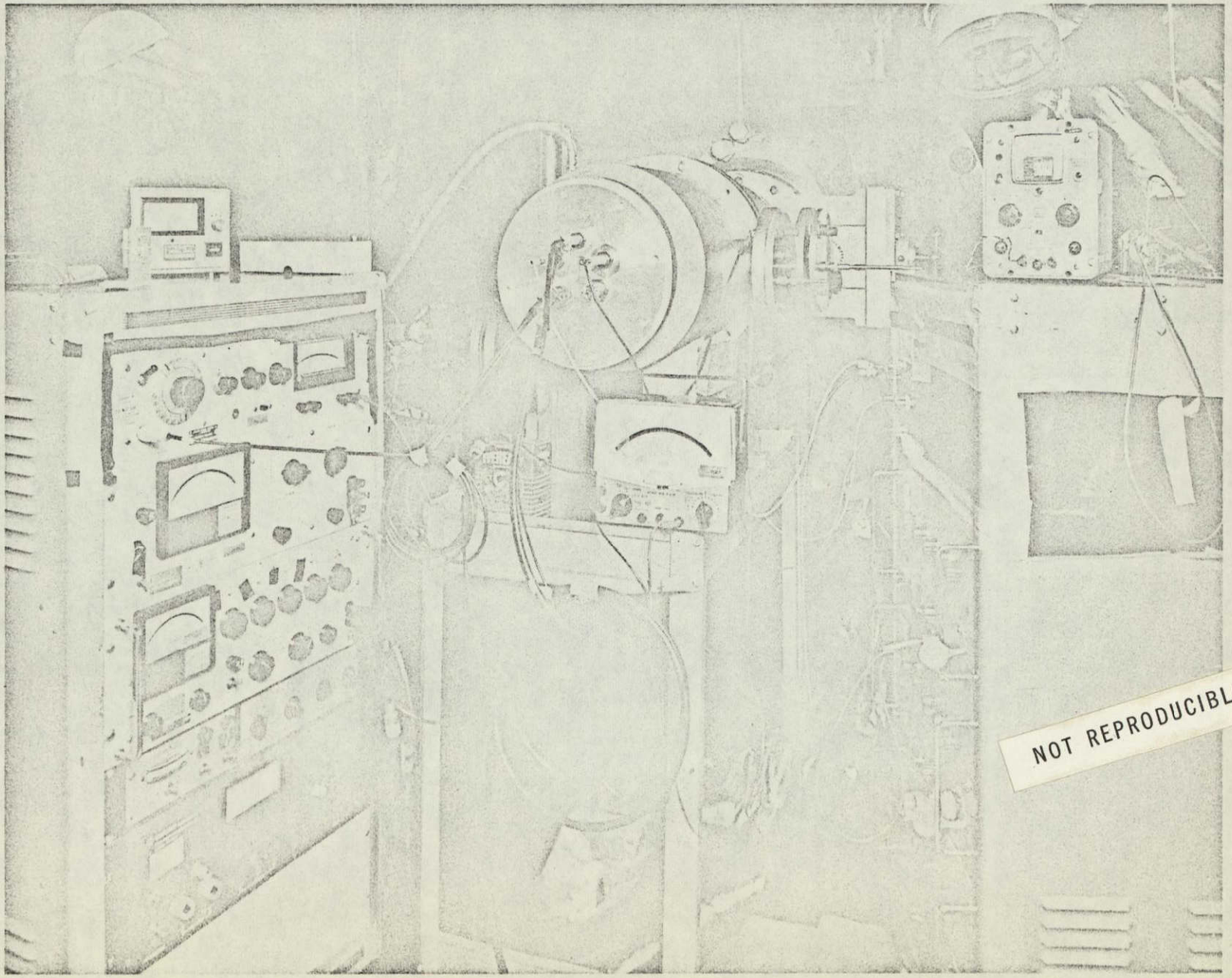

Figure 4-6. Portion of Spectrograph Mounted in Ante-Chamber Showing Subplatform

APPENDIX

THEORETICAL CONSIDERATIONS

PROCEDURE

Transfer matrix methods for calculating trajectories are well known in optics and have been applied to electron optics. The application of these methods to electrostatic and magnetic deflectors has been gaining increasing recognition in recent years. Consequently, they are particularly adaptable to the study of double-focusing mass spectroscopic instruments. The transfer matrices used in this study were taken from References 1 through 5.

Essentially, the transfer matrix approach is a method of ray tracing. For example, in the case of ion optics an element (e.g., an electric or a magnetic sector) is represented by a transformation (transfer matrix) which gives description to an ion beam which has traversed the element. In order to effect such a description, the ion beam is represented by a vector, the components of which are formed by the entrance slit dimensions, entrance angular spread, and the deviations in mass/charge ratio and energy. The total transfer matrix which describes the path of an ion beam from entrance slit to photographic plate is the product of as many as 11 individual matrices. Among these are included the important effects of the fringe fields of both the electric and the magnetic sectors and the effect of changing the sense of the beam deflection.

After the total transfer matrix (one each for radial and axial deflections) has been obtained, then the mass/charge dispersion, the magnification, and the first and second order aberration coefficients can be

identified. The axial aberrations are usually not considered past first order but the radial aberrations are calculated to second order and sometimes estimated to third order. In the present study, third order angle coefficients were included, and were assumed to have values 10 times that of the corresponding second order coefficients. The instrument resolution is calculated from elements of the total radial transfer matrix.

SIGNIFICANT ELEMENTS OF THE TOTAL RADIAL SECOND ORDER TRANSFER MATRIX

The total radial second order transfer matrix contains 289 elements of which only 17 are used in a determination of the resolving power of the instrument. These are given the notations as follows:

$$A_u,\ A_\alpha,\ A_\gamma,\ A_\delta,\ A_{uu},\ A_{u\alpha},\ A_{u\gamma},\ A_{u\delta},\ A_{\alpha\alpha},\ A_{\alpha\gamma},\ A_{\alpha\delta},\ A_{\gamma\gamma},\ A_{\gamma\delta},$$
$$A_{\delta\delta},\ A_{vv},\ A_{v\beta},\ A_{\beta\beta}$$

where α and β are the radial and axial half-angles, respectively. The quantities γ and δ are the mass/charge and energy deviations, respectively, defined as follows:

$$U = U_o[1 + \delta] \quad (1)$$

$$(M/Z) = (M/Z)_o[1 + \gamma] \quad (2)$$

where

- U - particle energy per unit charge
- U_o - particle energy per unit charge for central ray
- (M/Z) - particle mass/charge number
- $(M/Z)_o$ - particle mass/charge number with energy per unit charge U_o

The radial and axial displacements of the paraxial ray from the central ray are ur_m and vr_m where r_m is the radius of curvature of the central ray in the main magnetic field.

The most important of the 17 elements listed above are identified as follows:

- A_u - magnification
- A_α - first order radial angle aberration coefficient
- A_δ - first order energy aberration coefficient
- A_γ - mass dispersion coefficient
- $A_{\alpha\alpha}$ - second order radial angle aberration coefficient
- $A_{\alpha\delta}$ - second order radial angle-energy aberration coefficient
- $A_{\delta\delta}$ - second order energy aberration coefficient
- $A_{\beta\beta}$ - second order axial angle aberration coefficient

The third order coefficients of interest are:

- $A_{\alpha\alpha\alpha}$ - third order radial angle aberration coefficient
- $A_{\beta\beta\beta}$ - third order axial angle aberration coefficient

SIGNIFICANT ELEMENTS OF THE TOTAL AXIAL TRANSFER MATRIX

The axial transfer matrix first order elements are usually the only ones of interest and are denoted by:

- A_v - magnification
- A_β - first order axial angle aberration coefficient

INPUT PARAMETERS

The matrix elements are very lengthy, complicated functions of the input parameters. These parameters are given below:

- φ_m - magnetic sector angle
- φ_e - electric sector angle
- D - (separation between the electric and magnetic sectors) $\times 1/r_m$
- I'_α - parameter describing electric fringe field (input side)
- I''_α - parameter describing electric fringe field (output side)
- I'_β - parameter describing magnetic fringe field (input side)
- I''_β - parameter describing magnetic fringe field (output side)
- ϵ' - angle between the central ray and the normal to the input ideal field boundary of the magnetic sector
- ϵ'' - similar to ϵ' except refers to the output ideal field boundary of the magnetic sector
- c - parameter describing the inhomogeneity of the main electric field
- n - parameter describing the inhomogeneity of the main magnetic field
- $\bar{Q}'$ - [reciprocal radius of curvature of electric sector boundary (input side)] $\times r_m$
- $\bar{Q}''$ - [reciprocal radius of curvature of electric sector boundary (output side)] $\times r_m$
- $\bar{R}'$ - [reciprocal radius of curvature of magnetic sector boundary (input side)] $\times r_m$
- $\bar{R}''$ - [reciprocal radius of curvature of magnetic sector boundary (output side)] $\times r_m$
- r_e - radius of curvature of central path in the main electric field
- r_m - radius of curvature of central path in the main magnetic field
- sense - determines the relative deflections in the electric and magnetic sectors

COMPUTER METHODS

A computer program was written to evaluate the radial and axial transfer matrices for the complete system. This merely required doing a series of matrix multiplications, each matrix being the transfer matrix for a given region (i.e., fringing field region, electric sector region, etc.). Due to the rather large dimensions of the radial matrices (17 x 17), the evaluation of the complete radial transfer matrix required about 23 seconds on the CDC-3100 computer. The first row of this radial matrix then determined the image slit width (for a given object slit) in terms of the 15 parameters describing the system: c, n, φ_e, φ_m, ϵ', ϵ'', I'_α, I''_α, r_e/r_m, D, $\overline{Q}'$, $\overline{Q}''$, $\overline{R}'$, $\overline{R}''$, and INVERT. The first row of the 2 x 2 first order complete axial transfer matrix rendered the image slit length. Several cases were run this way in a sort of trial and error approach to finding a good set of system parameters, and it also served as a means of checking out the program for possible coding errors. Once the program was debugged, it was changed into a subroutine to be used by yet another bigger program. The purpose of this new program was to try and find a combination of the input (system) parameters that would result in an improvement over a set of "initial guess" parameters. The program operated as follows: An "error" function, ERROR, was invented. It essentially indicated the radial aberration of the image slit due to particles of incident angle (α) and energy deviation energy (δ). Thus:

$$\text{ERROR}\ (c, n, \varphi_e, \varphi_m, \epsilon', \epsilon'', r_e/r_m, D, \overline{Q}', \overline{Q}'', \overline{R}', \overline{R}'', \text{INVERT}) =$$
$$(2\alpha A_\alpha)^2 + (\alpha^2 A_{\alpha\alpha})^2 + (2\alpha\delta A_{\alpha\delta})^2 + (\delta^2 A_{\delta\delta})^2 + (2\delta A_\delta)^2$$

where the A's are the first row matrix elements of the complete radial transfer matrix. The values of α and δ were both arbitrarily set at 0.1.

The problem was now to minimize the ERROR function with respect to the various input parameters. (Actually, the parameters c, n, and INVERT were maintained at constant values and only the remaining 12 parameters were allowed to vary.) To find a minimum of a function, one merely computes the gradient of the function and then starts stepping backwards. This is exactly what was done. The 12 quantities:

$$\frac{\partial(\text{ERROR})}{\partial \phi e}, \quad \frac{\partial(\text{ERROR})}{\partial \phi m}, \quad \ldots, \quad \frac{\partial(\text{ERROR})}{\partial \bar{R}''}$$

were calculated. Then, the components of the normalized gradient were computed:

$$\frac{}{(\nabla \text{ERROR})_p} = \frac{\dfrac{\partial(\text{ERROR})}{\partial p}}{\sqrt{\sum_{k=1}^{12} \left[\dfrac{\partial(\text{ERROR})}{\partial p_k}\right]^2}}, \quad p = \phi e, \phi m, \ldots, \bar{R}''.$$

An initial step size of 1.0 was chosen and this amount was "stepped off" in the direction of the negative gradient. (Note: this step was taken in 12-space; not on each parameter; consequently, each parameter changed by considerably less than 1.0 per step.) After each step the gradient was again re-computed to determine the direction in which the next step should be made. This process continued as long as the value of ERROR continued to decrease. Then, when a step in the direction of $-\nabla(\text{ERROR})$ finally resulted in "going uphill", it was reasoned that a minimum had been overshot. So, the step size was reduced by a factor of 10 and the search continued at this smaller step size.

This above process was to continue until the step size became less than a certain value (about 0.001), at which point the minimum of the ERROR function would be claimed and the search would be over.

Unfortunately, things did not work completely according to plan. After the first "over-shooting" of the minimum with a step size of 1.0 it would seem plausible that by reducing the step size to 0.1 the minimum should be over-shot again within about ten steps at most. This never happened. Instead the step-off would continue in units of 0.1 well past the expected 10 iterations. It is difficult to say just how long this step size would continue to last since the time estimate of the program would always be exceeded, even when more than 1 1/2 hours was allowed. The main problem with the program was the amount of time it took. Since each evaluation of a gradient required an evaluation of the complete transformation matrix 12 times (one for each parameter), the time required for just one iteration step was almost 5 minutes! However, a later feature of the program allowed any of the parameters to be held fixed while the rest varied. This helped to increase the iteration frequency, although no minimum as such was ever found within the 99 minutes of time allotted per computer run.

RESOLUTION CLOSE TO THE CENTRAL RAY POINT AT THE IMAGE PLANE

Resolution (R), as described in Fig. 1, is defined as follows:

$$R = \frac{M/Z}{\Delta(M/Z)} \quad \text{or} \quad \frac{1}{2\gamma} \tag{3}$$

This is the resolution which can be obtained close to the central ray point of the image plane and is given analytically by the following expression:

$$R = \frac{0.5\, r_m\, \Lambda_\gamma}{S'\Lambda_u + r_m\left[2\alpha\Lambda_\alpha + 2\delta\Lambda_\delta + \alpha^2\Lambda_{\alpha\alpha} + 2\alpha\delta\Lambda_{\alpha\delta} + \delta^2\Lambda_{\delta\delta} + \beta^2\Lambda_{\beta\beta} + 2\alpha^3\Lambda_{\alpha\alpha\alpha} + 2\beta^3\Lambda_{\beta\beta\beta}\right]} \tag{4}$$

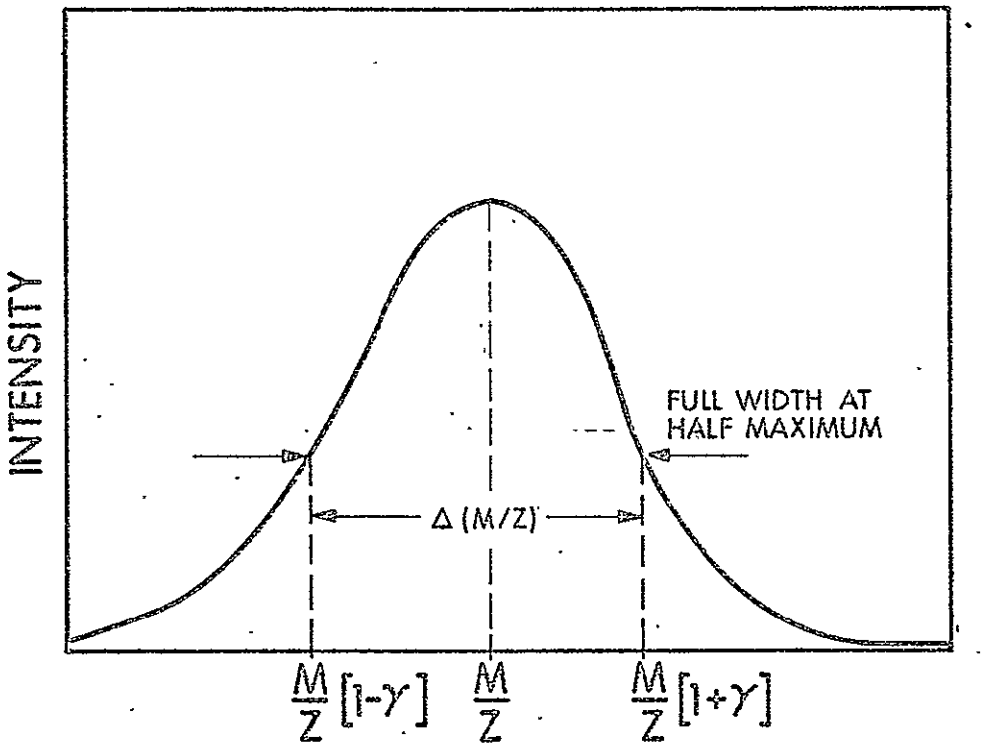

Figure 1. Definition of Resolution

where the values of all coefficients are taken as absolute. That is, minus signs are ignored. The S' $(=2u_o r_m)$ is the width of the entrance slit (object). It should be noted that the length of the entrance slit is $2v_o r_m$.

Ideally, the best instrument design would be one for which all the aberration coefficients (except A_u and A_γ) vanished simultaneously. As can be seen in Eq. 4, it is desirable for A_γ to be as large as possible, and A_u to be minimized to less than unity.

DOUBLE-FOCUSING CONFIGURATIONS

The aberration coefficients for about 650 configurations were calculated. Most of these were slight modifications of a set of initial conditions on the parameters. In no case were the coefficients pertaining to α and δ made to assume insignificantly small values, simultaneously. During the study, values of the coefficients were observed to range from 10^{-5} to over 100. Figure 2 shows the notation scheme of design parameters.

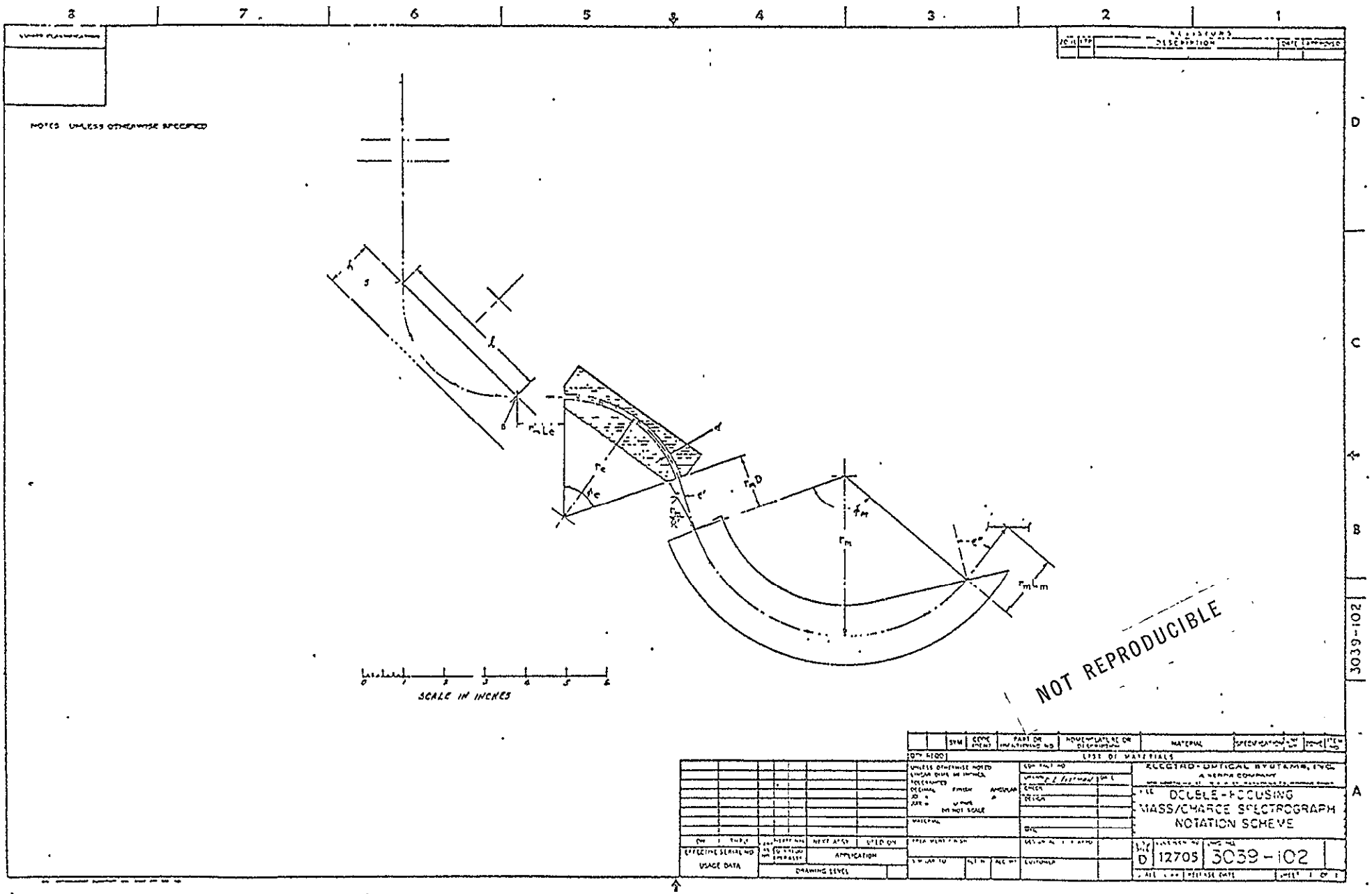
NOTES UNLESS OTHERWISE SPECIFIED
SCALE IN INCHES
NOT REPRODUCIBLE
ELECTRO-OPTICAL SYSTEMS, INC.
A XEROX COMPANY
DOUBLE-FOCUSING
MASS/CHARGE SPECTROGRAPH
NOTATION SCHEME
D 12705 3039-102
3039-102

Figure 2.

REFERENCES

1. H. Wollnik, Nucl. Instr. and Meth. 52, 250-272 (1967)
2. H. Wollnik, Nucl. Instr. and Meth. 34, 213-221 (1965)
3. H. Wollnik, Nucl. Instr. and Meth. 59, 277-282 (1968)
4. H. Wollnik, Nucl. Instr. and Meth. 53, 197-215 (1967)
5. H. Wollnik, Nucl. Instr. and Meth. 36, 93-104 (1965)